

ALMA MATER STUDIORUM
UNIVERSITÀ DI BOLOGNA

Dottorato di Ricerca in Fisica
XXIX Ciclo

Settore Concorsuale di afferenza: 02/A1

Settore Scientifico Disciplinare: FIS/01

**Study for a real-time alert system
for multi-messenger astronomy with the
KM3NeT/ARCA neutrino telescope**

Presentata da: **Dr. Carmelo Pellegrino**

Coordinatore Dottorato:
Prof. Gastone Castellani

Relatore:
Prof.ssa Annarita Margiotta
Correlatore:
Dott. Tommaso Chiarusi

Esame finale anno 2017

*“Study and in general the pursuit
of truth and beauty is a sphere
of activity in which we are permitted
to remain children all our lives.”*
A. Einstein

Introduction

Neutrino astronomy is a frontier research field within particle astrophysics that exploits neutrinos produced during violent cosmic events as an astronomical probe.

Since the mists of time, the sky has been an inexhaustible source of mystery and fascination. The knowledge of mankind has reached about astrophysical phenomena and structures has grown exponentially, starting from the simple observation of stars and constellations with naked eye to the Galileo's optical telescope, to gamma, neutrino and, very recently, to the gravitational detectors.

Neutrino telescopes are designed to detect high-energy cosmic neutrinos allowing to reveal their source direction.

The study of the Universe through the electro-magnetic radiation may be hindered by the Nature itself. For example, the infra-red (IR) and the cosmic microwave background radiation (CMBR) put hurdles in the detection of very high-energy γ -rays, that are largely absorbed within few Mpc.

The use of charged particles as an astronomical probe is discouraged by the effect of galactic and extragalactic magnetic fields, that makes impossible to reveal the exact source direction up to extreme high energies ($\sim 10^{18}$ eV). Anyhow, above this limit, the flux is extremely low and, moreover, interactions with the CMBR start to take place, limiting the astronomical horizon to few 10 Mpc.

The origin, sources and acceleration mechanisms of such charged cosmic rays represent some of the big open questions in astroparticle physics. Is the high-energy cosmic γ production linked to the acceleration of ultra high-energy cosmic rays (UHECR)?

Since neutrinos could be produced in the environment surrounding the acceleration site and being only weakly interacting, they represent the optimal probe for the extreme high-energy events in the Universe. They can travel enormous distances without interactions, neither with the matter nor with the cosmic radiation, thus preserving the direction of the source, and can escape very dense objects, providing direct information about the mechanisms acting in their core.

Together with the development of neutrino astronomy, multi-messenger studies can amazingly improve our knowledge, possibly answering to the

above questions. The coincident detection of a high-energy neutrino flux together with a highly-energetic astrophysical event both, coming from the same direction, could represent the so-called “*smocking gun*” for UHECR sources.

In this thesis, a new alert system for multi-messenger studies with the ARCA KM3NeT neutrino telescope is presented. The key features of this system, namely *ANTS*, are the efficiency and speed in reconstructing the source direction of astrophysical neutrino candidates, together with high background rejection power.

The structure of the thesis is the following: the basics of neutrino astronomy and detection are discussed in chapter 1 and chapter 2, respectively. Chapters 3 and 4 are dedicated to the KM3NeT detector and to its trigger and data acquisition system (TriDAS). The ANTS system and its characterisation are presented in chapter 5 and chapter 6.

Contents

Introduction	i
1 Cosmic rays	1
1.1 Cosmic rays	1
1.1.1 Acceleration of Cosmic Rays	5
1.2 Neutrino sources	6
1.2.1 Galactic sources	8
1.2.2 Extragalactic sources	9
1.2.3 Diffuse neutrino sources	11
2 Neutrino astronomy	13
2.1 Astronomy with neutrinos	13
2.1.1 Neutrino interaction	13
2.1.2 Čerenkov neutrino detection	16
2.1.3 Alternative neutrino detection techniques	17
2.1.4 Neutrino event signatures	18
2.2 Neutrino telescopes	21
2.2.1 DUMAND	22
2.2.2 Baikal	22
2.2.3 IceCube	22
2.2.4 ANTARES	24
2.2.5 NEMO	25
2.2.6 NESTOR	27
2.2.7 KM3NeT	27
3 KM3NeT	29
3.1 The Detection Unit	31
3.2 The Digital Optical Module	32
3.3 Background sources	35
3.3.1 Optical background	35
3.3.2 Atmospheric muons and neutrinos	36
3.4 Networking infrastructure	37

4	Trigger and Data Acquisition System for KM3NeT	39
4.1	TriDAS design	39
4.1.1	On-line software	39
4.2	Trigger system	44
4.2.1	T-Triggers	45
4.2.2	Simple Causality filter	45
4.2.3	Sky Scan trigger	45
4.2.4	Tracking trigger	45
4.2.5	Vertex Splitting trigger	47
4.2.6	External trigger	48
5	ANTS: Astrophysical Neutrino Trigger System	49
5.1	Multi-messenger astronomy	49
5.2	Description of the system	50
5.2.1	Reconstruction algorithm	52
5.2.2	Trigger system	59
6	Characterisation of ANTS	61
6.1	Monte Carlo	61
6.2	Reconstruction	63
6.2.1	Purity	65
6.2.2	Efficiency	68
6.2.3	Angular resolution	69
6.2.4	Performances	72
	Conclusions	75
	Bibliography	77
	Appendix A	a
	Appendix B	e

Chapter 1

Cosmic rays

1.1 Cosmic rays

In 1912, Victor Hess, using golden electrometers in free balloon flights, discovered the presence of ionising radiations in the Earth's atmosphere [1]. Its intensity increases with altitude, proving that it is originated from outside the Earth.

These radiations are widely referred to as *cosmic rays* (CR). Despite this name, the cosmic rays discovered by Hess were actually particles produced by the interaction of particles of higher energy with the nuclei of the topmost part of the Earth's atmosphere. Usually they are referred to as *secondary cosmic rays*, the *primaries* being the high-energy particles of cosmic origin.

Until the development of accelerator physics, cosmic rays were an invaluable source for particle physics studies. The positron [2], the muon [3] and the pion [4] were discovered in cosmic rays, as well as other heavier particles.

The energy spectrum of primary cosmic rays ranges from 10^9 to $\sim 10^{20}$ eV. About 90% of the CRs arriving at the top of the Earth's atmosphere are protons; α -particles constitute about 9% of the total, while the rest is given by heavier nuclei, electrons and γ -rays. A small quantity of antimatter is also present. The elemental composition of CR radiation is quite similar to what is observed in the Solar System, with some evident differences, as shown in figure 1.1: Li-Be-B and Sc-Ti-V-Cr-Mn are more abundant in cosmic rays than in the Solar System by several orders of magnitude. These elements, not directly produced by stars, are created by spallation processes of heavier elements in the interstellar medium: Carbon, Nitrogen and Oxygen give origin to the first group, while Iron accounts for the second one [6].

Below $\sim 10^{14}$ eV, direct chemical composition of CR is measured with satellite and balloon experiments. At higher energies, only indirect measurements are possible because the cosmic rays flux is too low to collect enough statistics.

As a first approximation, the primary energy spectrum, shown in figure

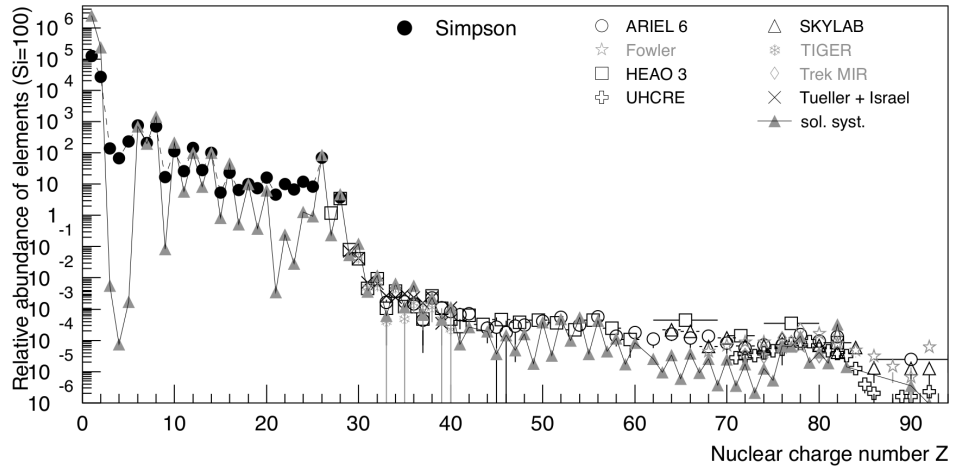


Figure 1.1: Comparison between the elemental composition in cosmic rays and in the Solar System, normalised to the abundance of silicon [5].

1.2, exhibits an unbroken power-law trend for almost the whole range:

$$\frac{dN}{dE} \propto E^{-\gamma} \quad (1.1)$$

Two changes of the slope are, however, evident in the measured spectrum: around 10^{15} eV (the *knee*) and above $10^{18.5}$ eV (the *ankle*). The names come from the similarity of the shape of the spectrum with the human leg. The spectral index γ has approximately the value of 2.7 up to the knee, where the spectrum sharpens to a value of $\gamma \sim 3.1$. Then, a flattening is present at the ankle, where $\gamma \sim 2.7$.

The origin of the steepening in the knee region is still an open question: many models have been proposed to explain it [8]. A dependency of the maximal energy on the charge of particles at the main galactic acceleration sites (probably supernovae remnants, discussed in subsection 1.2.1) could translate into different values of a cut-off energy for each nuclear species and would be visible in a transition from a *proton-rich* to an *iron-rich* composition at the knee. A different class of galactic objects is expected to accelerate cosmic rays above the knee. Details on cosmic rays acceleration mechanisms are discussed in subsection 1.1.1. Figure 1.3 shows a collection of results on the cosmic ray spectrum measurement above 1 TeV. The spectrum is here multiplied by $E^{2.5}$ to emphasise its features. After the knee, the ankle is visible around $10^{18.5}$ eV, where the spectrum flattens. This feature is usually attributed to a transition from galactic to extragalactic sources of cosmic rays [9]. A harder spectrum is indeed expected for extragalactic CRs.

An upper limit to the energy of detectable cosmic rays is given by the so-called Greisen-Zatsepin-Kuz'min (GZK) effect [10, 11], that is discussed

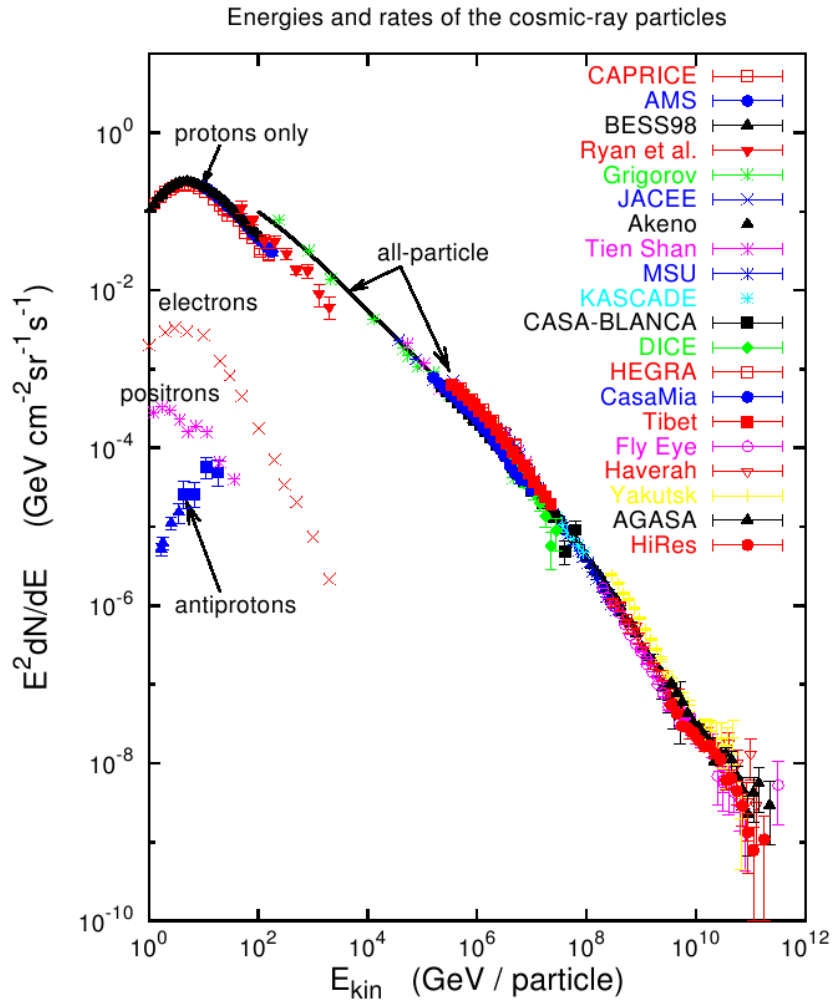


Figure 1.2: Cosmic ray energy spectrum from 1 to 10^{12} GeV as measured by different experiments, either on balloons, satellites and ground-based as in the legend [7]. The spectrum is multiplied by E^2 to better show the knee, the ankle and a ultra high-energy cut-off.

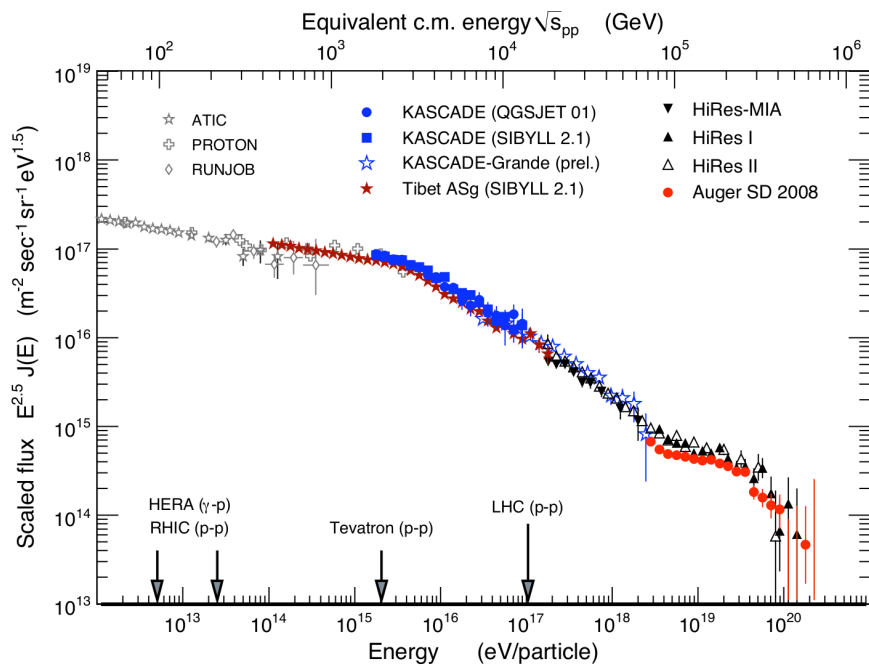


Figure 1.3: Collection of measurement of the CR energy spectrum above 1 TeV [5]. The spectrum is multiplied by $E^{2.5}$ in order to show its features in shape such as the knee, the ankle and the high-energy cut-off.

in section 1.2.3.

The arrival direction of cosmic rays at the top of the atmosphere is isotropically distributed. The presence of galactic ($\simeq 4 \mu\text{G}$) and extragalactic ($\simeq \text{nG}$) magnetic domains randomly bends the trajectory of charged particles. The Larmor radius:

$$R_L = \frac{mv_{\perp}}{eB} \quad (1.2)$$

of a proton moving at speed \vec{v} in the galactic magnetic field \vec{B} , where v_{\perp} is the modulus of the particle velocity in the plane orthogonal to the magnetic field, becomes compatible with the thickness of the Milky Way ($\simeq 200 \div 300 \text{ pc}$ [12]) only above 10^{18} eV . Particles of lower energy or higher charge are confined in the Galaxy and randomly deflected many times in the irregularities of the magnetic field. This reflects in the fact that only very high-energy charged cosmic rays or neutral ones can point back to their sources.

The interaction of a primary cosmic ray with nuclei in the Earth's atmosphere produces extensive air showers (EAS) of particles. Very large ground array detectors, observing the products of cosmic rays interactions in the atmosphere, can indirectly infer the mass of the primary nucleus. These indirect measurements seem to suggest that, beyond the knee, cosmic ray composition becomes heavier [8]. These results are however strongly dependent on the model of the hadronic interactions and a precise determination of the composition is difficult. Highly energetic muons and neutrinos, relic of air showers, constitute the most important source of signal-like background in underwater telescopes.

1.1.1 Acceleration of Cosmic Rays

The first attempt to model the acceleration mechanism of cosmic rays was done by Enrico Fermi in 1949 [13]. Despite the fact that Fermi's model was correctly predicting a power-law spectrum, a satisfactory model for cosmic rays acceleration was hypothesized by Tony Bell in 1978 [14]. In the original Fermi's model, a charged particle gains energy by interacting with magnetic ripples in interstellar clouds; the energy gain in each interaction is proportional to the square of the velocity of the cloud in the observer's rest frame. Conversely, in the Bell's model, the interaction with astrophysical shock waves is considered. They are huge matter waves produced in the proximity of black holes or Super Novae explosions. The gas in the shock is more dense and hotter than the surrounding interstellar medium and moves at a larger speed than the speed of sound in the local medium. By iterative stochastic interactions with the wave front of the shock, a relativistic charged particle reaches extreme energies. In each iteration, the energy of the particle increases by a quantity $\Delta E = \epsilon E$, where ϵ is proportional to the velocity of the shock wave. For this reason the Bell's model is often referred to as *Fermi first order acceleration*, while the original Fermi's is called the *Fermi*

second order acceleration.

The first order mechanism leads to an unbroken energy spectrum ($\propto E^{-\gamma}$) with spectral index $\gamma \sim 2$. The difference with the observed index $\gamma \sim 2.7$ can be explained by considering the confinement by the galactic magnetic field [12]. The last consideration does not apply to neutrinos that should maintain the same spectral index as in the production environment.

The maximum energy that can be reached at an accelerator is, intuitively, given by its power and its capability to confine the cosmic ray within the acceleration region. The capability to stifle a particle is proportional to both the magnetic field and the size of accelerator. The *Hillas plot* (figure 1.4) shows the relation between size and magnetic field of accelerator. At a fixed size of the acceleration site, the higher the intensity of the magnetic field is, the longer is the CR confinement within its surrounding and can be further accelerated via Fermi mechanisms. Analogously, at a given magnetic field intensity, the larger the site is, the more encounters with the accelerating shocks are possible. Finally, a more compact object would require a higher magnetic field intensity to accelerate a CR to the same energy as a larger source. Moreover, the presence of a relativistic shock, with high Lorentz boost factor, can produce a further enhancement of the CR energy.

1.2 Neutrino sources

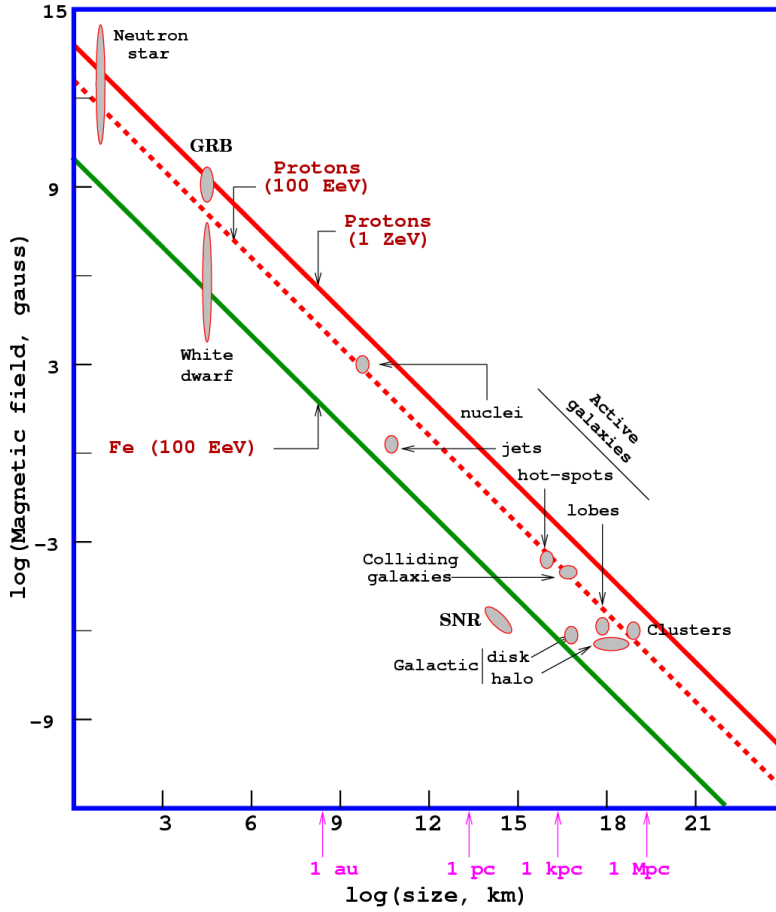
In the following sections, the classes of astrophysical objects which are supposed to be responsible for both cosmic rays accelerations and high energy neutrino emission are discussed. Such objects have been discovered and studied through their photon emission in a wide band of wavelength, from infra-red (IR) to γ .

The physical processes responsible for high-energy electromagnetic emission can be grouped into two main groups:

- the *leptonic* scenario: high-energy electrons produce radiation via inverse-Compton on ambient photons or synchrotron effect in the local magnetic field;
- the *hadronic* scenario: the astrophysical source is also a powerful hadron accelerator; high-energy photons come from the decay of the neutral pions ($\pi^0 \rightarrow 2\gamma$) that are abundantly produced in hadronic interactions.

High-energy neutrinos may come from the decay of high-energy charged pions or neutrons, as described in equation 1.4 and equation 1.5.

Hillas-plot
(candidate sites for $E=100$ EeV and $E=1$ ZeV)



$$E_{\text{max}} \sim ZBL \quad (\text{Fermi})$$

$$E_{\text{max}} \sim ZBL\Gamma \quad (\text{Ultra-relativistic shocks-GRB})$$

Figure 1.4: The Hillas plot (drawn by Murat Boratav) schematically summarises the properties of acceleration sites, i.e. size and magnetic field strength, for a given maximal energy of a cosmic ray. Sources above the red solid (dashed) line can accelerate protons up to 1 ZeV (10^{21} eV). The green line refers to the acceleration of Iron nuclei up to 100 EeV.

$$\pi^{+(-)} \rightarrow \mu^{+(-)} + \nu_{\mu}(\bar{\nu}_{\mu}) \quad (1.3)$$

$$\begin{array}{c} \downarrow \\ \bar{\nu}_{\mu}(\nu_{\mu}) + \nu_e(\bar{\nu}_e) + e^{+(-)} \end{array} \quad (1.4)$$

$$n \rightarrow p^+ + e^- + \bar{\nu}_e \quad (1.5)$$

A coincidence detection of neutrino and γ emission from an astrophysical object would be a proof of the hadronic scenario.

Under the assumption of production via pion decay, the expected neutrino flavour ratio at the source is $\nu_e : \nu_{\mu} : \nu_{\tau} = 1 : 2 : 0$. However, neutrino oscillations in vacuum over cosmic distances let the ratio to become uniform to an equal composition of $1 : 1 : 1$ [15]. For this reason, all neutrino flavours are expected to arrive at Earth.

1.2.1 Galactic sources

After a supernova explosion, the emitted material encounters the interstellar medium and a shock front is built. This shock front forms a part of the *Supernova Remnant* (SNR). Charged particles are accelerated in shock waves of the expanding shells via the first order Fermi mechanism. The maximum energy that a SNR can accelerate to a nucleus with charge equal to Ze is given by [12]:

$$E_{\text{SNR}}^{\text{max}} \sim 300 \cdot Z \text{ TeV} \quad (1.6)$$

This is the energy of the first change of slope in the cosmic ray energy spectrum. The transition over the knee can thus be explained as a dependency on Z of the maximal energy cosmic rays can be accelerated to by SNRs (figure 1.5).

Beyond the energy threshold for SNRs, different mechanisms, providing further particle acceleration, must be taken into account. This is possible, for example, when a Neutron Star (NS) with a strong magnetic field is present in the SNR environment. This works as an additional particle accelerator. These objects are also called *Pulsar Wind Nebulae* (PWNe). Indeed, the magnetic field of the NS is often misaligned with respect to its rotation axis. Spinning magnetic fields can produce strong electric fields according to the Faraday's law. Given the strong intensity of the magnetic fields around the neutron star, few of these systems can provide enough energy to fill the Galaxy with cosmic rays up to 10^{18} eV.

Further galactic candidate CR accelerators are *micro-quasars*, where a compact object accretes stealing material from a normal star. The in-falling matter releases gravitational potential energy. Due to this enormous motion

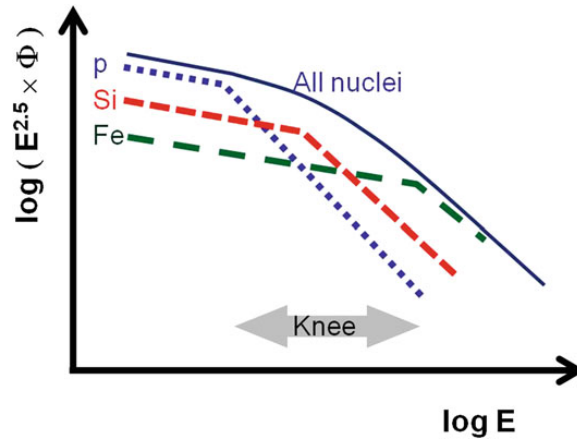


Figure 1.5: Elemental composition of cosmic rays at the knee. The change in the slope is supposed to be due to the galactic accelerators energy limits, that depends on the charge (Z) of the nucleus. The flux of each nuclear species sharply decreases after a given cut-off depending on Z . The behaviour of hydrogen, silicon ($Z = 14$) and iron ($Z = 26$) nuclei are shown [12].

of ionized matter, very strong electromagnetic fields are produced in the proximity of the compact object and charged particles can be accelerated to high energies. Most galactic objects which could accelerate CRs are located in the Galactic Plane, where the highest density of SNRs, PWNe and micro-quasars is present.

1.2.2 Extragalactic sources

Gamma Ray Bursts

A *Gamma Ray Burst* (GRB) is an astrophysical phenomenon characterized by a short and intense *flash* of light in the γ -spectrum. GRBs were first discovered by the American VELA spy satellites in 1967, which had been designed to detect covert nuclear weapons tests. Thanks to the Beppo-SAX satellite, launched in 1996 to study the Universe in the X- and γ -bands, the correlation between the GRBs and the subsequent *afterglows* in the X-ray (see figure 1.6) and optical bands was studied. Then, Earth based measurements have revealed that GRBs are produced in extragalactic environments (redshift $\simeq 0.0085 \div 9$).

The energy release by a GRB event is between 10^{51} and 10^{54} erg¹ in a bulk time period between 0.1 and 10 seconds. According to the duration of the burst they are classified as either *short* or *long* corresponding to durations below or above few seconds, respectively. Short GRBs are believed to be originated by the merging of two compact objects, like two neutron

¹1 erg = 10^{-7} J $\simeq 6.2 \cdot 10^{11}$ eV

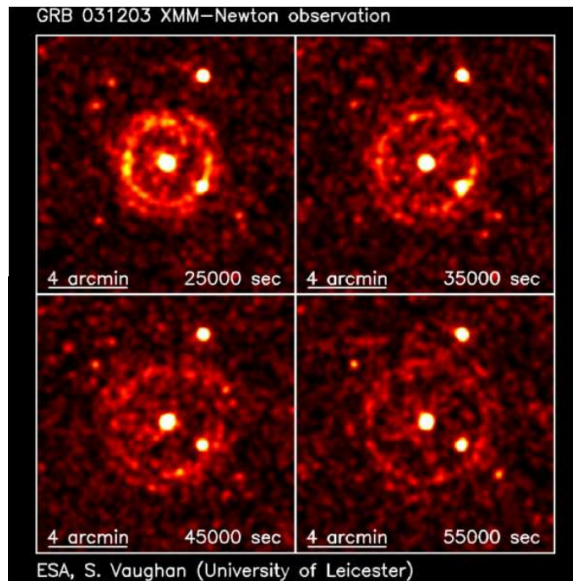


Figure 1.6: Time evolution of GRB 031203 taken by the XMM-Newton space telescope. Credits Simon Vaughan, <http://www.star.le.ac.uk/~sav2/grb031203/>.

stars or a neutron star and a black hole. Since compact objects are involved, γ -ray emissions have a short duration. Long GRBs can be produced in the supernova collapse of extremely massive stars. In both cases the steady γ -emission and the subsequent afterglow can be described by the fireball model. The central engine, activated by a huge release of gravitational energy, can produce a jet of highly relativistic material, with Lorentz boost larger than $100 \div 200$ [16]. This jet, moving through a dense environment, produces shocks that emit γ -rays by synchrotron processes and inverse Compton effect. The afterglow emission, at higher wavelengths, is caused by the time-delayed interaction of the jet with the surrounding medium. Since large and extremely fast shock waves are produced, cosmic rays can be accelerated during GRB events. The high Lorentz boost of the shock can enhance the maximal energy of accelerated particles up to the highest end of the cosmic rays spectrum.

Active Galactic Nuclei

Active Galactic Nuclei (AGN) are the most powerful continuously emitting energy sources in the Universe. The emitted power is usually in the range $10^{42} \div 10^{43}$ erg/s. They were first observed by Carl Seyfert in 1943 [17]. He found that some galaxies exhibit a high luminosity coming from their centre in a broad band of wavelength. A super massive black hole (SMBH, $M_{\text{SMBH}} = 10^6 \div 10^9 M_{\odot}$) sited at the centre of a galaxy becomes visible thanks to the emissions from matter falling into it from an accretion

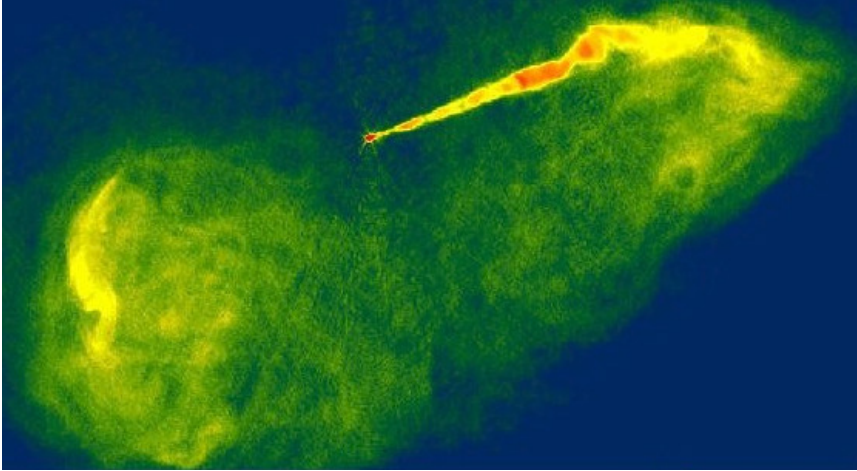


Figure 1.7: Astrophysical jet going out from NGC 4486 (Virgo A), a giant elliptic galaxy in the Virgo Cluster. The image has been taken by the Very Large Array (VLA) radio telescope in February 1989 in the radio spectrum. A super massive black hole ($M \simeq 6.6 \cdot 10^9 M_{\odot}$) is present at the centre of the galaxy [18].

disk. Due to the enormous magnetic field, two jets of particle and radiation can be emitted. The AGN becomes even more luminous than its host galaxy if one of the jets is in the line of sight of the observer.

A large variety of objects is nowadays classified as AGN. The unified model for AGNs [19, 20] explains the large variety of observed features considering that same kind of objects can be seen from different angles. Because of the presence of emission jets and shocks in the galactic and extragalactic medium, AGNs are candidate engines for cosmic rays to the most extreme energies. So far, no correlation between the arrival direction of UHECRs and AGNs has been found [21].

1.2.3 Diffuse neutrino sources

GZK

Immediately after the discovery of the cosmic microwave background radiation (CMBR) in 1966, Zatsepin together with Kuz'min[11] and Greisen [10] had speculated about a strong suppression of the flux of cosmic protons starting from a certain energy threshold. This expected feature of the cosmic ray spectrum is called *GZK cut-off*.

The cross-section of the proton-photon interaction increases dramatically at $\sqrt{s} \approx 1232 \text{ MeV}$ due to the Δ^+ resonant production. Considering the average energy of a CMBR photon in our rest frame ($E_{\text{CMBR}} \simeq 1.2 \text{ meV}$), the proton energy threshold is roughly $E_{th} = 5 \cdot 10^{19} \text{ eV}$.

Given the peak cross-section ($\sigma \approx 0.3$ mbarn) and the density of CMBR photons ($\rho \approx 400/\text{cm}^3$) [12], the mean free path of a proton at the energy threshold is approximately:

$$\lambda_{\text{GZK}} \simeq \frac{1}{\rho \cdot \sigma} \simeq 20 \text{ Mpc} \quad (1.7)$$

For this reason, only protons from the Milky Way and the Local Group galaxies are expected to be detected above the GZK threshold.

Many experiments have measured a cut-off in the cosmic ray spectrum at the highest energies [22, 23, 24], but some tension is still present in the interpretation of this feature.

The GZK effect is also a source of the so-called diffuse *cosmogenic* neutrinos. Among the Δ^+ decay modes, the *neutron+pion*, shown in equation 1.8, provides particles decaying as shown in equation 1.4 and equation 1.5.



Chapter 2

Neutrino astronomy

2.1 Astronomy with neutrinos

Due to the presence of galactic and extragalactic magnetic fields, charged particles do not point back to their sources up to extreme energies. Cosmic rays below 10^{18} eV, the highest expected for a CR accelerated in our Galaxy, are deflected by galactic magnetic fields.

Neutral particles originating from prompt interactions of CRs with the medium surrounding their accelerator carry direct information from their origin, unaffected by magnetic fields. Those are neutrons, γ -rays and neutrinos. Since neutrons are short-lived they cannot reach the Earth to be detected. The γ -rays are generally absorbed in the inter-stellar medium and, moreover, photons with energy greater than 1 TeV start interacting with the cosmic microwave and infra-red background radiation via electron-positron pair production [25]. Neutrinos are the only known particles that can travel through the Universe without interacting.

The observation of neutrinos from an individual cosmic object would be the *smoking gun* of cosmic ray acceleration taking place at that particular astrophysical site.

The detection of neutrinos is done by revealing the products of their interaction with matter. In the following sections a brief description of the *signatures* of neutrino interactions is provided.

2.1.1 Neutrino interaction

Weak interaction processes are grouped into two categories: *Neutral Current* (NC) processes, where the interaction is mediated by a Z^0 boson; *Charged Current* (CC) processes, where the mediator of the interaction is a W^\pm boson. The NC processes are characterized, due to the lack of charge exchange, by the presence of a neutrino in the final states. Conversely, in the CC processes, a charged lepton is produced in the final state.

$$\nu_l + X \rightarrow \nu_l + Y \quad (\text{NC}) \quad (2.1)$$

$$\nu_l + X \rightarrow l + Y \quad (\text{CC}) \quad (2.2)$$

In processes 2.1 and 2.2, l is one of the possible leptonic flavours: e for electron, μ for muon and τ for tau, X is a nucleon, and Y represents the final hadronic state.

The differential cross-section for neutrino-nucleon interaction is [26, 27]:

$$\frac{d^2\sigma}{dx dy} = \frac{2G_F^2 M E_\nu}{\pi} \left(\frac{M_B^2}{Q^2 + M_B^2} \right)^2 [xq(x, Q^2) + x\bar{q}(x, Q^2)(1-y)^2] \quad (2.3)$$

where M_B is the mass of mediator boson, $M_W \simeq 80.38 \text{ GeV}$ or $M_Z \simeq 91.19 \text{ GeV}$ for charged or neutral current processes, respectively, $G_F \approx 1.16 \cdot 10^{-5} \text{ GeV}^{-2}$ is the *Fermi's weak coupling constant*, M is the nucleon mass, $-Q^2$ is the invariant momentum transfer between the incident neutrino and the out-going lepton, E_ν is the energy of incident neutrino, $q(x, Q^2)$ and $\bar{q}(x, Q^2)$ are the quark and anti-quark distribution functions. Finally, x and y are the Bjorken scaling variables:

$$x = \frac{Q^2}{2M\epsilon} \quad (2.4)$$

$$y = \frac{\epsilon}{E_\nu} \quad (2.5)$$

$\epsilon = E_\nu - E_l$ being the energy difference between the in-coming neutrino and the out-going lepton.

Figure 2.1 shows the ν_μ and $\bar{\nu}_\mu$ cross-sections as a function of the neutrino energy. The cross-section follows a power-law shape (E^Γ) with spectral index Γ equal to 1 up to some tens of TeV, where it flattens to about 0.4 because the square of the transferred momentum Q^2 becomes larger than M_B^2 . Large theoretical uncertainties are present since few measurements are available for parton distribution functions at small x , corresponding to high energies, thus only extrapolations are possible.

The average inelasticity, $\langle y \rangle$, is the fraction of the energy of the incoming neutrino gained by the out-coming lepton:

$$E_l = \langle y \rangle \cdot E_\nu. \quad (2.6)$$

It is a function of E_ν and its dependency is shown in figure 2.2, for both CC and NC interactions of neutrinos with nucleons. It slightly decreases as the energy increases from 0.3 (anti-neutrino) and 0.5 (neutrinos) to ≈ 0.2 at 10^{10} GeV . A high-energy muon from muon neutrino CC interaction would retain from half to one fifth of the original neutrino energy.

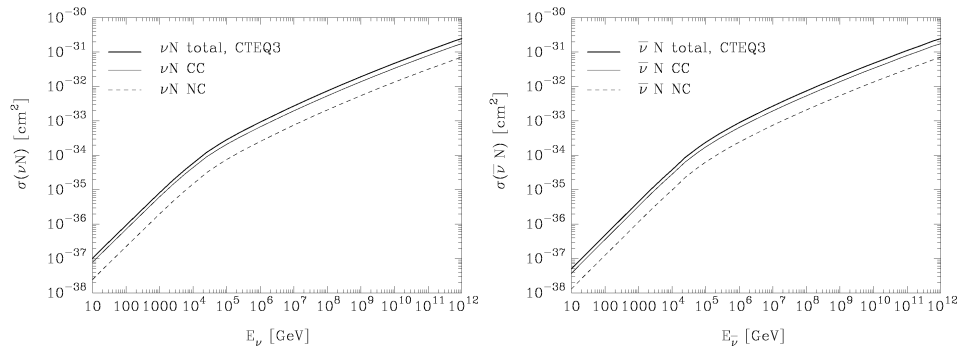


Figure 2.1: Integral neutrino (left) and anti-neutrino (right) cross-sections with nucleons [26].

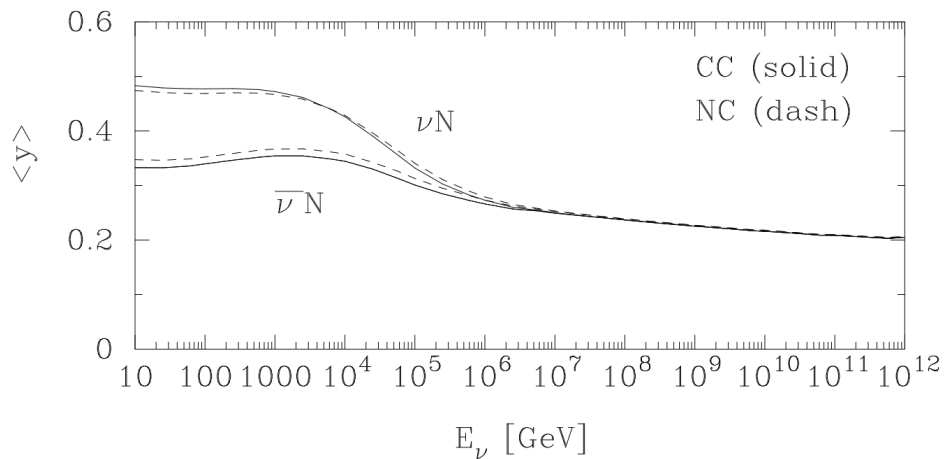


Figure 2.2: Energy dependence of the inelasticity parameter $\langle y \rangle$ for CC (solid lines) and NC (dashed lines) interactions as a function of the incident neutrino energy [26].

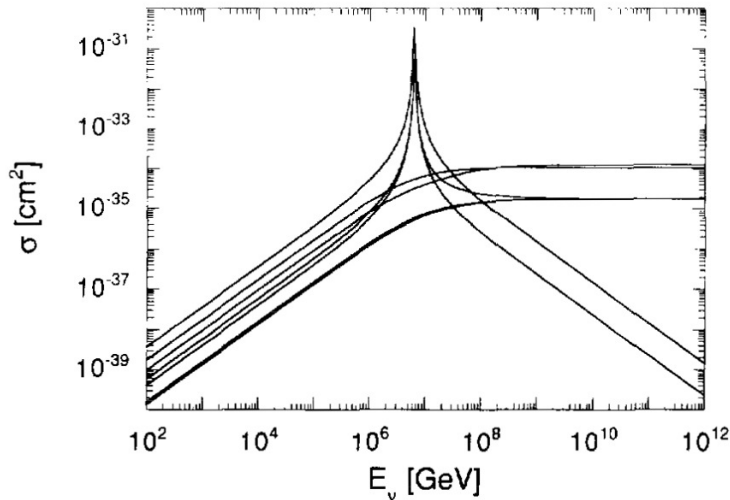


Figure 2.3: Integral anti-neutrino cross-sections with electron. At low energy, from the higher to the lower cross-section: $\bar{\nu}_e e^- \rightarrow \text{hadrons}$, $\nu_\mu e^- \rightarrow \mu^- \nu_e$, $\nu_e e^- \rightarrow \nu_e e^-$, $\bar{\nu}_e e^- \rightarrow \bar{\nu}_\mu \mu^-$, $\bar{\nu}_e e^- \rightarrow \bar{\nu}_e e^-$, $\nu_\mu e^- \rightarrow \nu_\mu e^-$, $\bar{\nu}_\mu e^- \rightarrow \bar{\nu}_\mu e^-$. The central peak at $E_\nu \approx 6.3 \cdot 10^6$ GeV corresponds to the Glashow resonance of the W^- boson [26].

Neutrino-electron interactions can generally be neglected with respect to neutrino-nucleon interactions [28], apart in the case of resonant formation of the intermediate boson W^- in $\bar{\nu}_e + e^- \rightarrow W^-$ interactions at 6.3 PeV (Glashow's resonance) [29]. Figure 2.3 shows the integral cross-section of electron and muon (anti-)neutrinos with electron.

2.1.2 Čerenkov neutrino detection

A charged particle that moves faster than the speed of light in a medium produces, along its path, photons via the Čerenkov effect [30]. Indeed, the charged particle polarises the molecules along its trajectory, producing an overall dipole moment. Light is emitted when the electrons of the medium restore themselves to equilibrium after the disruption has passed, producing coherent radiation. This radiation is emitted at a characteristic angle, θ_C with respect to the direction of propagation of the charged particle, given by:

$$\cos \theta_C = \frac{1}{\beta \cdot n} \quad (2.7)$$

where n is the refractive index of the medium and β is the particle speed in units of c . For highly relativistic particles ($\beta \simeq 1$) in sea water ($n \simeq 1.364$), the Čerenkov angle is about 43° . The number of Čerenkov photons, N , emitted per unit wavelength interval $d\lambda$ and unit distance travelled dx , by a

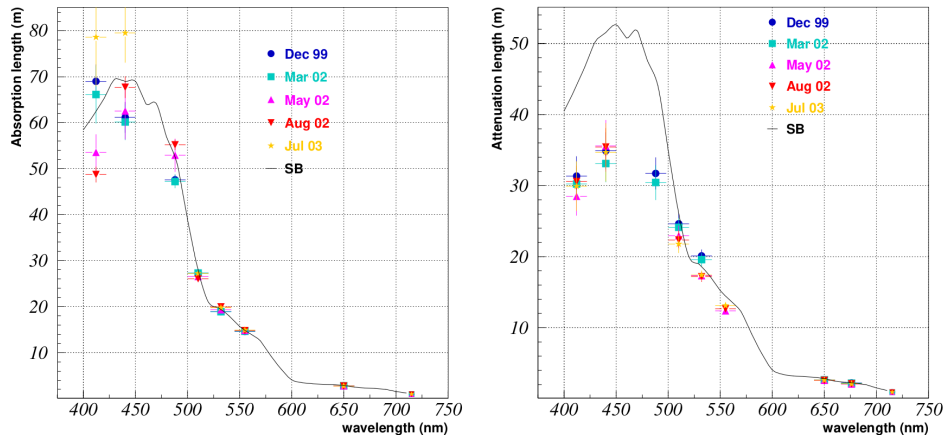


Figure 2.4: Average absorption (left) and attenuation (right) lengths measured with the Capo Passero site, at depth $2850 \div 3250$ m in December 1999 (blue circle), March 2002 (light blue square), May 2002 (purple triangle), August 2002 (red upsidedown triangle) and July 2003 (dark yellow star). Solid black lines indicates the values for optically pure seawater [32].

charged particle of charge Ze is given by the Frank-Tamm formula [31]:

$$\frac{d^2N}{dx d\lambda} = \frac{2\pi\alpha Z^2}{\lambda^2} \left(1 - \frac{1}{n^2\beta^2}\right) \quad (2.8)$$

where α is the fine-structure constant. For underwater detectors, Čerenkov radiation is significant in the wavelength range between 300 and 600 nm (visible, near UV). In such range, the number of Čerenkov photons emitted per metre along the path of a 1 TeV muon (charge $|Z| = 1$) is about $3.5 \cdot 10^4$. In figure 2.4, the light absorption coefficient in water is shown as a function of the wavelength. In the aforementioned range the light can go through several tens of metres in water.

2.1.3 Alternative neutrino detection techniques

Apart from the Čerenkov technique, successfully used by the IceCube [33], ANTARES [34] and Baikal [35] experiments, alternative neutrino detection techniques exist. Despite the fact that their development is still in a embryonic state, they could represent a promising future extension for the existing experiments.

Radio detection

A particle moving at a speed greater than the phase speed of light in a dense dielectric material can produce an electromagnetic shower that contains a charge anisotropy and thus emits a cone of coherent electromagnetic

radiation in the radio or microwave spectrum, in a way similar to the Čerenkov effect. This phenomenon, firstly postulated by Gurgun Askaryan in 1962 [36], can be exploited to detect high-energy cascades ($E \geq 10^{15}$ eV) in salt, ice or in the lunar regolith. The effect was first observed experimentally in 2000, 38 years after its theoretical prediction. So far, the effect has been observed in silica sand [37], rock salt [38], and ice [39] in accelerator experiments.

The intensity of the signal is proportional to the square of the energy of the shower, while the frequency depends on its length.

Askaryan radio effect can be exploited to build neutrino detectors in ice [40]. Indeed, a shower of charged particles can be produced by the interaction of high-energy ν . As a consequence Askarian radiation is emitted. The absorption length of \sim GHz radio waves is of the order of some kilometres. Few tens of radio antennas can thus serve as enormous detector surfaces. Thermal radio background in ice determines an experimental limit for radio detectors that have better sensitivity with respect to the optical Čerenkov technique starting from some PeV of neutrino energy [41]. The IceCube collaboration is studying the possibility to extend the detector with an array of radio antennas, called IceRay [42] that would increase the effective volume.

Acoustic detection

A high-energy neutrino interacting in water produces showers of particles. A macroscopic amount of energy is released in a very short time thus producing a sudden overheating of the water smitten by the shower. This adiabatic process converts the heat into a mechanical wave through the so-called *thermo-acoustic effect*, theorized by Askaryan in 1957 [43]. The acoustic signal can propagate for several kilometres in sea water, allowing a sparse detector to have a big effective volume [44].

An array of acoustic sensors properly distributed in a big volume of sea water can detect and reconstruct the wave front of the neutrino acoustic signal. This technique is sensitive to any neutrino interaction process as it aims at detecting a shower of particles. Anyway, the acoustic background present in sea water sets a neutrino energetic threshold of $\simeq 10^{16}$ eV, rather higher with respect to the one for Čerenkov detection.

This detection technique has been proposed for improving the performances of the KM3NeT detector and has been tested by the AMADEUS apparatus in the ANTARES detector [45].

2.1.4 Neutrino event signatures

Muon detection

A high-energy muon is produced during the CC interaction of a high-energy muon neutrino with matter. The direction of the μ is highly correlated

with that of neutrino and the angle between the two is [46]:

$$\theta_{\nu\mu} \simeq \frac{0.6^\circ}{\sqrt{E_\nu(\text{TeV})}} \quad (2.9)$$

Assuming that the muon energy is well above the Čerenkov emission threshold, the detection of these photons allows the reconstruction of its direction and consequently that of the neutrino. High-energy muons can be well reconstructed since they travel straight through the detector, producing a clear track signature.

Muons lose energy because of ionisation, pair production, bremsstrahlung and photo-nuclear interactions. The energy loss per unit path length can be parametrised as [47]:

$$-\frac{dE_\mu}{dx} = \alpha(E_\mu) + \beta(E_\mu) \cdot E_\mu \quad (2.10)$$

where $\alpha(E_\mu)$ describes the ionisation loss, slightly depending on the muon energy, while $\beta(E_\mu)$ describes the radiative losses: pair production, bremsstrahlung and photo-nuclear interactions. Typical values are $\alpha \approx 0.2 \text{ GeV/m}$ and $\beta \approx 4 \cdot 10^{-4} \text{ m}^{-1}$ in water. Given the Čerenkov energy threshold for a muon, $\tilde{E} \simeq 60 \text{ MeV}$, the muon track length of a muon in water is:

$$L = \int dx = \int_{\tilde{E}}^{E_{th}} \left(-\frac{dE}{dx} \right)^{-1} dE = \frac{1}{b} \ln \frac{a + b\tilde{E}}{a + bE_{th}} \quad (2.11)$$

that leads to a Čerenkov-detectable track length of 2.7 km for a 1 TeV muon.

Figure 2.5 shows the *effective range* of muons, among others, in water. This quantity is the distance after which a muon of initial energy, E_μ , is still above the energy threshold, E_μ^{th} , for detection in the apparatus. A 10 TeV atmospheric muon can reach a detector sited 4 km below the sea level with an energy above 1 TeV. The event is observed even if the neutrino interaction vertex is far from the instrumented volume, increasing the effective size of the detector.

Shower detection

In a ν interaction, hadronic and electromagnetic showers can be produced. If the vertex of the interaction is contained inside the active volume, also NC and ν_e CC interactions can be detected. In ν_e CC, an electromagnetic (EM) shower is produced since a high-energy electron is induced by the neutrino interaction. This electron can radiate bremsstrahlung γ -rays, again producing e^+e^- pairs and generating a further cascade of EM particles. As long as the charged particles in the EM showers are above the Čerenkov threshold, light is emitted. Hadronic showers are represented by the term, Y , of equations 2.1 and 2.2 and are present in both CC and NC interactions.

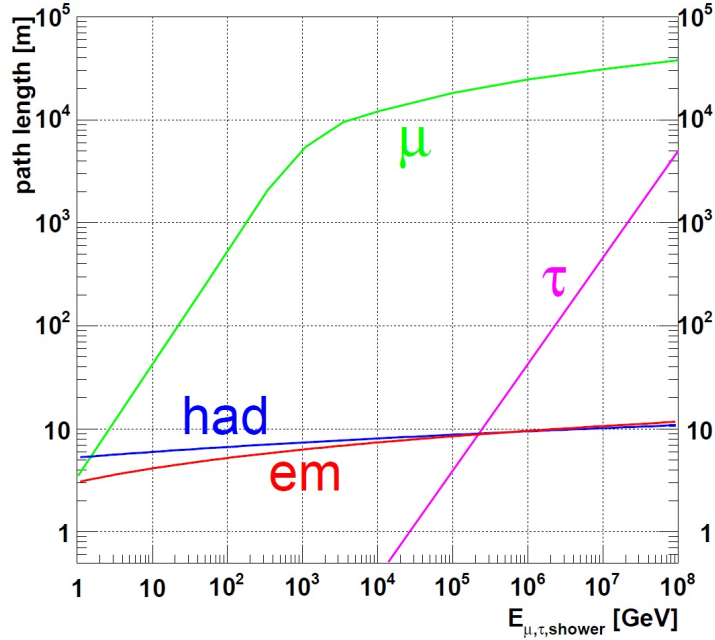


Figure 2.5: Path length in water of particles produced in neutrino interaction.: muons (μ), taus (τ), electromagnetic (γ and electrons, em) and hadrons (had) as a function of their energy [12].

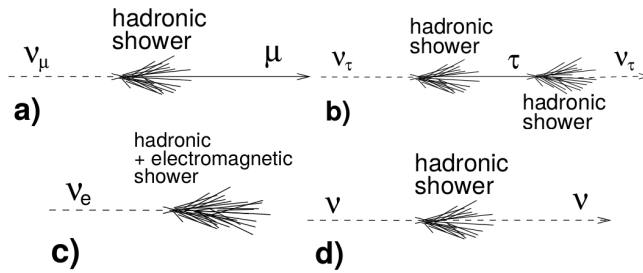


Figure 2.6: Event signature topologies for different neutrino flavours and interactions: a) CC interaction of a ν_{μ} produces a muon and a hadronic shower; b) CC interaction of a ν_{τ} producing a τ which then decays, tracing the double bang event signature; c) CC interaction of ν_e produces both an EM and a hadronic shower; d) a NC interaction produces a hadronic shower [12].

The largest contribution to hadronic showers is given by pions, but also other mesons and baryons can be produced. An electromagnetic component is present in the hadronic shower because π^0 mesons immediately decay into 2γ . All the particles in a hadronic shower can produce additional particles via radiation mechanism which further interact with the medium. Until the charged particles in the cascade are above the speed of the light in the medium, detectable Čerenkov light is produced. Shower events are usually be characterised by an expanding spherical shell of light, centred around the shower maximum. Also in this case, the shower direction can be reconstructed and correlated to the neutrino arrival direction.

Tau detection

A ν_τ CC interaction produces a τ lepton. Tauons are short-lived leptons ($2.9 \cdot 10^{-13}$ s) and preferably decay into hadrons ($\text{BR}(\tau \rightarrow \nu_\tau + \text{hadrons}) \approx 64\%$ [48]). At high energies, their Lorentz factor can be large enough to produce a visible τ track before the lepton decays. In this case, shower-like events are present at the interaction vertex and at the decay point. A track-like event would also be visible since the tau lepton produces Čerenkov light. Below 1 PeV, the interaction vertex hadronic shower and the decay shower are too close to be distinguished in a sparsely instrumented volume. At higher energies and for large detectors, the two showers can be separated and a *double bang event* – each *bang* corresponding to a shower – is detected. If one of the two showers, either the interaction or the decay one, is outside the detection volume, only a track and a cascade are visible producing a so-called *lollipop event*.

2.2 Neutrino telescopes

In 1961, Moisey Alexandrovich Markov [49] proposed the idea of modern neutrino telescopes. Due to the feeble flux and the small cross-section of high-energy neutrinos, enormous quantity of target material must be used. The only affordable solution is to exploit natural distributions of transparent media like sea water or polar ice. Installing a lattice of optical sensors deep under the sea or a lake or even under the polar permanent ice makes these large portions of transparent medium sensitive to the passage of Čerenkov photons emitted along the path of high-energy charged particles originated by cosmic neutrino interactions. Installing the detector deep in water or ice also provides an effective shield from atmospheric muons, that constitute the main source of background events. Indeed, the Earth’s crust is a favourable target for neutrino interaction, being denser than the water and, moreover, allows perfect shielding from atmospheric muons.

In the following sections an overview of past and current experiments is presented.

2.2.1 DUMAND

The first attempt to implement Markov's idea is represented by the Deep Underwater Muon And Neutrino Detector (DUMAND) project [50], that aimed at building a neutrino telescope in the Pacific Ocean. The detector design foresaw the installation of both optical detectors and *hydrophones*¹ to implement both the Čerenkov and acoustic technique. The DUMAND project started in 1976 but was cancelled by U.S. Department of Energy in 1995 due to technical difficulties. Preliminary studies were carried in order to deploy a detection unit in the Pacific Ocean, off Hawaii Islands, at a depth of about 4800 m. Even though DUMAND did not reach its final construction phase because of technical and financial problems, all the subsequent projects took advantage of the experience gained from its R&D phase.

2.2.2 Baikal

The lake Baikal, located in Russia, is one of the most extensive lakes in the world and the deepest. Starting from 1993, at a depth of about 1.1 km, it hosts the NT-200 detector, consisting of 192 optical modules [51]. Preliminary measurements in the search for high-energy neutrinos have been completed [52] and cubic kilometre volume detector, GVD, is foreseen to be built in the next years adjacent to NT-200 [53]. A thick ice shell is present on the lake during the winter time and allows to easily deploy instruments in the water. Low optical background is expected in fresh water with respect to sea water but the water of Lake Baikal is less transparent than sea water or ice, limiting the reconstruction performance.

2.2.3 IceCube

IceCube is the first km³ neutrino Čerenkov detector ever built [54]. It consists of 86 strings, each instrumented with 60 digital optical modules (DOM), spaced up to 17 m apart over a total length of one kilometre. The strings, installed via hot water drills, are arranged in a hexagonal pattern with 125 m average spacing between neighbouring strings. Eight of the deployed strings fill in a central volume between standard strings and create the most densely instrumented DeepCore region. The detector comprises 5160 *photo-multiplier tubes* (PMTs) installed at depths between 1450 and 2450 metres in the Antarctic ice. A drawing of the IceCube array is shown in figure 2.7.

The first observation ever made of a cosmic neutrino signal has been reported by the IceCube collaboration in the High Energy Starting Events (HESE) analysis in 2013 [55, 56]. Since then, IceCube has collected independent evidences for an astrophysical neutrino signal by analysing different

¹An hydrophone is a special device that acts as a microphone. It suited to work deep into liquids and at high static pressure with high amplitude resolution.

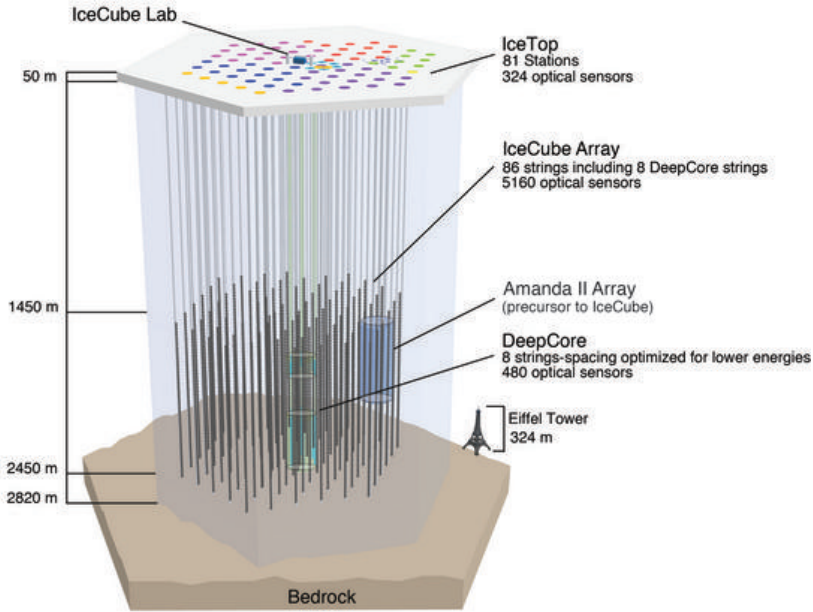


Figure 2.7: Sketch of the IceCube telescope [33].

event signatures including shower-like and starting events at lower energies (≥ 30 TeV) as well as track-like events that interact outside the detector with zenith angle $> 85^\circ$, called *through-going* events [57].

By means of a vetoing system, using the outer layers of the detector, the atmospheric muons can be rejected in IceCube. This allows the selection of a cosmic neutrino sample coming from the whole sky, not limiting the analysis to upward-going event. Indeed, above 100 TeV, Earth absorption strongly reduces the number of high-energy neutrinos, limiting the possibility of observing an high-energy neutrino signal as upward-going track-like events. The IceCube HESE sample is dominated by downward-going events.

A measurement of the cosmic neutrino flux has been produced by the IceCube collaboration for $E_\nu > 25$ TeV [58]:

$$\frac{d\Phi_\nu}{dE} = (2.3 \pm 0.4) \cdot 10^{-18} \cdot \left(\frac{E^{-2.6 \pm 0.15}}{\text{TeV}} \right) \text{GeV}^{-1} \text{s}^{-1} \text{cm}^{-2} \text{sr}^{-1} \quad (2.12)$$

A search for the neutrino sources has been performed but no statistical significance, neither in spatial nor in time of these events, has been found [57], as shown in figure 2.8.

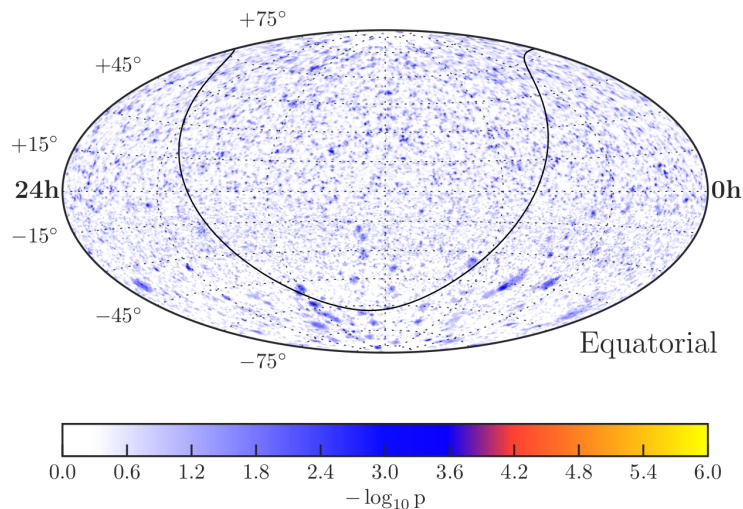


Figure 2.8: Map of p-values representing the local probability that an excess of events at a given position in the sky is due to a fluctuation of the expected background [59].

2.2.4 ANTARES

The ANTARES (*Astronomy with a Neutrino Telescope and Abyss environmental RESearch project*) [34] detector is the first operational neutrino telescope in the Mediterranean Sea. It is made of about 900 PMTs, installed within a volume of $\sim 0.1 \text{ km}^3$, 40 km off Toulon (France, see figure 2.10), at a depth of 2475 m below the sea level in the Ligurian Sea. It is active, in its final configuration, since 2008. Large area PMTs ($10''$ diameter) are arranged along 12 vertical lines (or *strings*) and grouped in 25 equidistant *storeys*, hosting 3 optical sensors each. Figure 2.9 shows an artistic view of the telescope.

The PMTs are downwards oriented, “looking” at 45° with respect to the vertical in order to favour the detection of upward-going Čerenkov light. The distance between adjacent lines is about 60 metres, while the distance between adjacent storeys is 14.5 metres. Each line is about 450 metres high and the first floor is about 100 m above the sea bed. A 42 km electro-optical cable guarantees the connection between the detector and the shore station, located at La Seyne-sur-Mer. Through this cable both the power feed and the bidirectional data communication are provided.

The underwater sea environment is a critical aspect of the experiment. The detector components must resist to the enormous pressure and to the presence of salt in water that chemically attacks the metals.

In order to minimise the complexity and thus the risk of harmful failures, the electronics is kept at the minimum requirements for what concern power

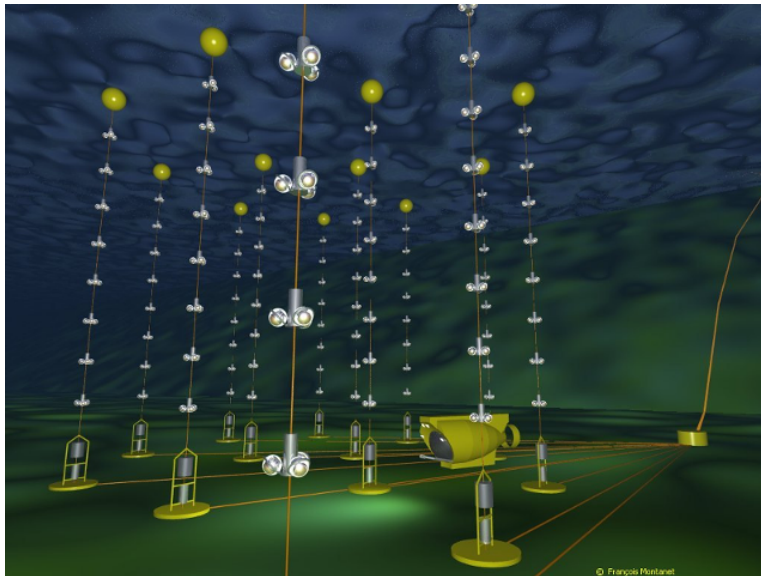


Figure 2.9: Artistic picture of the ANTARES telescope by François Montanet.

consumption and number of components. Indeed, the *all-data-to-shore* approach is used: the off-shore electronics does not perform any special processing, that is demanded to the on-shore computing infrastructure.

Being in the Mediterranean Sea, the detector has a good visibility of the Southern sky and can exploit the reconstructed tracks of upward-going neutrino-induced muons to identify possible sources with a very good angular resolution. This is the most interesting region for cosmic neutrino searches due to the presence of the Galactic Centre and Galactic Plane, where many neutrino emitting candidates could be located.

2.2.5 NEMO

The NEutrino Mediterranean Observatory (NEMO) [60] was a project financed by the Italian Institute of Nuclear Physics (*Istituto Nazionale di Fisica Nucleare*, INFN) (see figure 2.10). As for the other underwater telescopes, the optical modules are arranged into 700 m high vertical structures, here called *towers*. A NEMO tower is made of 14, 8 m long horizontal bars, piled up one by one with 90° heading difference. Each bar hosts 6 OMs, each of them containing a 10" PMT and the readout electronics, and two hydrophones serving a multidisciplinary observatory for underwater acoustics [44, 61] and the acoustic positioning system [62]. The OMs are placed in groups of two at the bar ends and at the centre, as shown in figure 2.11. Indeed, the towers move under the effect of undersea currents and a continuous monitoring of their position must be done. A general overview of the NEMO project is given in [63]. Two detector prototypes were built and deployed in 2006 and

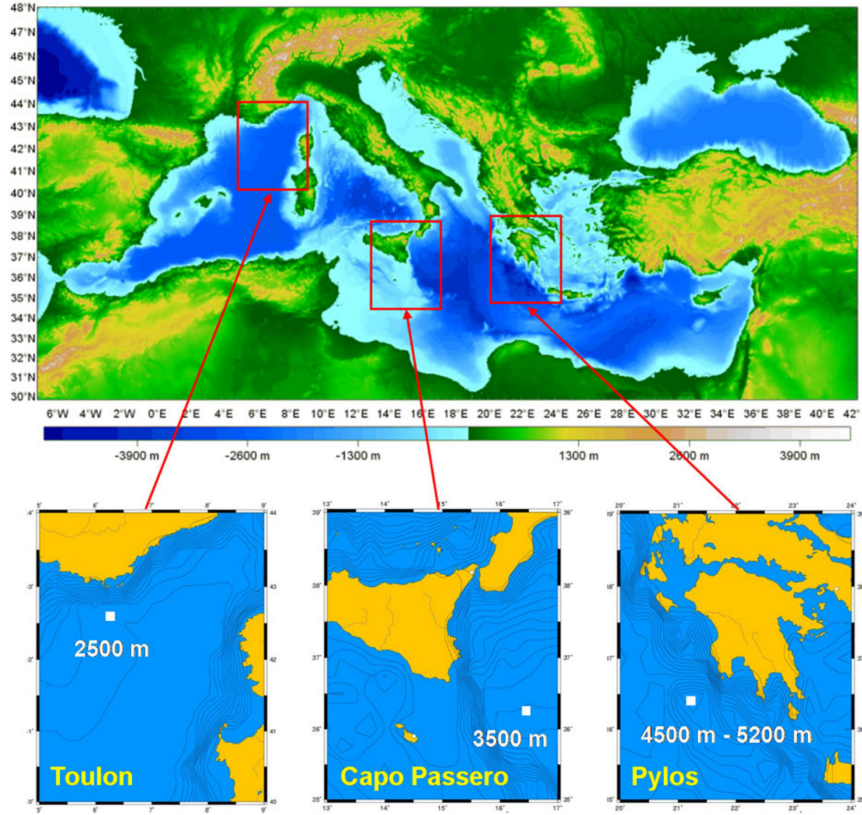


Figure 2.10: Installation sites for the KM3NeT telescope. \triangle : in the Ligurian Sea (Toulon) site, currently hosting the ANTARES telescope, will be installed the ORCA detector. \square : West Ionian Sea (Portopalo di Capo Passero) is the site selected by the NEMO Collaboration and will host the ARCA telescope. \circ : in the East Ionian Sea (Pylos) was foreseen the construction of the NESTOR telescope.

2013, named Phase I and II, respectively.

The Phase I prototype is a tower made by 4 bars, hosting 4 OMs at the two ends, pointed downwards and horizontally. It was installed in the test site near the city of Catania, 25 km away from the coast at a depth of 2100 m. Phase I allowed to test the technology developed by the NEMO collaboration.

The Phase II detector consisted of 8 bars, still in the 4 OMs configuration and two hydrophones each. It was installed in the Portopalo di Capo Passero site in March 2013 and successfully operated for 500 days. It proved the quality of the R&D studies made by the collaboration. The collected data allowed to extend the knowledge about the *Deep Intensity Relation* (DIR) of the atmospheric muons in water, as shown in figure 2.12 [64].

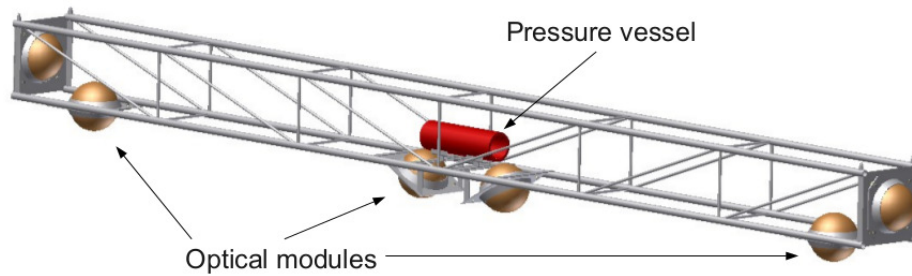


Figure 2.11: Scheme of a NEMO bar. The OMs are placed at the two ends and at the centre. The more extreme PMTs are oriented horizontally, looking outwards. The PMTs at the centre, inclined by 45° with respect to the horizontal, are down-looking. Last two PMTs look downward. The pressure vessel hosts the control and power electronics, and the fibre optic link system.

2.2.6 NESTOR

The Neutrino Extended Submarine Telescope with Oceanographic Research (NESTOR) was the first project operating in the Mediterranean Sea. The selected installation site was located at a depth of 3800 m under the sea level in the East Ionian Sea, off the city of Pylos in Greece. Semi-rigid 360 metres high *tower* made of 14 storeys was consisting the detection unit. Each storey was a rigid structure with the shape of a Star of David. At each of the 6 ends two PMTs were hosted, for a total of 168 in a tower.

In March 2003, a prototype 12 metres single-storey detection unit was deployed and started taking data [65] for about one month, before the electro-optical cable broke up.

2.2.7 KM3NeT

Starting from 2008, the ANTARES, NEMO and NESTOR collaborations joined their forces into the KM3NeT project. A detailed description is in chapter 3.

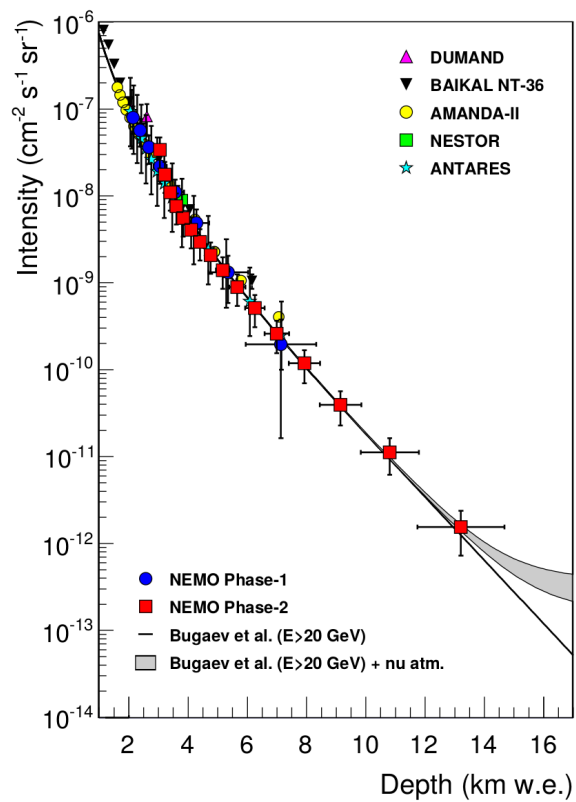


Figure 2.12: Intensity of atmospheric muon as a function of the depth, in km of water equivalent, as measured by different under-water experiments [64].

Chapter 3

KM3NeT

The km^3 *Neutrino Telescope* (KM3NeT) [66, 67, 68] is a network of new generation underwater neutrino detectors being installed in two sites in the Mediterranean Sea: off Toulon, France, at a depth of about 2500 m the *ORCA* (Oscillation Research with Cosmics in the Abyss) detector is devoted to the study of neutrino mass hierarchy, exploiting neutrinos produced in atmospheric extensive air showers; off Portopalo di Capo Passero, Sicily, at a depth of 3500 m, the *ARCA* (Astronomy Research with Cosmics in the Abyss) detector aims at performing astronomic studies by means of high-energy cosmic neutrinos. The positions of the sites are shown in figure 2.10. KM3NeT design is based on the ANTARES experience, and taking advantage of the work done with the NEMO project. The present thesis focuses on the ARCA detector. For details about ORCA the reader can refer to references [67, 69].

The basic element of both ARCA and ORCA detectors is the *Digital Optical module* (DOM) [70], shown in figure 3.2. It is a 17” pressure-resistant diameter glass sphere containing 31 3” photomultiplier tubes, a piezo-electric acoustic sensor for positioning purposes, and the read-out and digital transport electronics together with a set of environmental sensors [71]. Each site of the KM3NeT detector comprises thousands of DOMs arranged into linear structures, called Detection Units (DUs) or *strings*, kept vertical by a system of buoys exploiting the Archimede’s force. A standard KM3NeT string hosts 18 DOMs, vertically spaced by 36 (9) metres in the ARCA (ORCA) configuration. This difference comes from the optimisation studies of the detector, reflecting the different ν energy range being studied. Indeed, to measure low-energy neutrinos, a “dense” detector is required, while for high-energy cosmic neutrino detection, large volumes are mandatory due to the low flux but “sparse” sensor distribution is sufficient and more cost-affordable.

The development of KM3NeT follows a phase-based work plan as reported in table 3.1.

A *building block* is a detector made of 115 strings and, in the case of

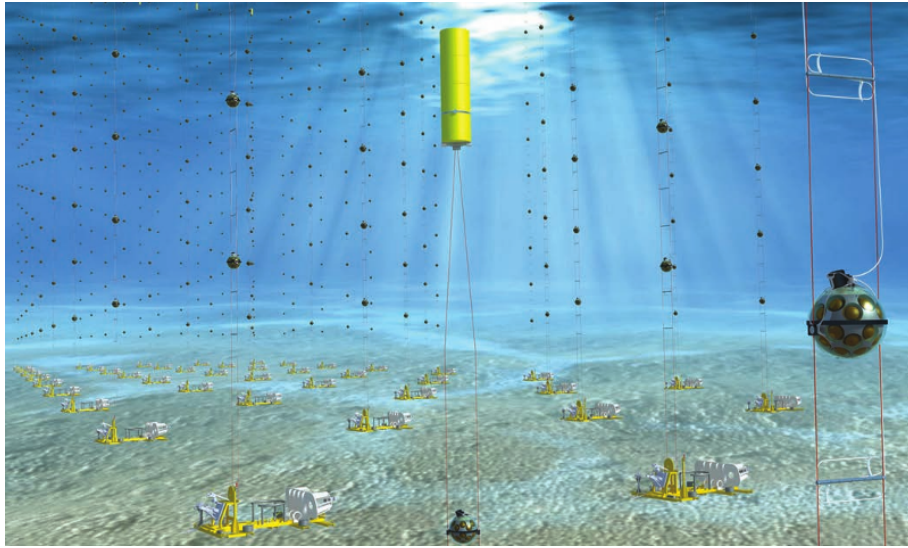


Figure 3.1: Pictorial view of a KM3NeT detector. The underwater environment is actually in a deep darkness.

Phase	Number of strings	Start	Deliverables
1	ARCA 24	2015	Proof of feasibility and first science results.
2	ARCA 230 ORCA 115	2017	Study the neutrino signal reported by IceCube. Determination of the neutrino mass hierarchy.
3	ARCA 575	2025	Neutrino astronomy including Galactic sources

Table 3.1: Work plan of the KM3NeT development. The implementation and completion of the ORCA detector is foreseen during the Phase-2 [67].

ARCA, covers a $\sim 0.5 \text{ km}^3$ instrumented volume. Two building blocks are planned to constitute the Phase-2 ARCA detector. A high-energy muon producing an event on one building block should not be registered by the other. Also the distance between the two building blocks has been chosen in order to optimise this aspect. This allows to effectively double the effective area covered by the full detector with respect to a single larger building block.

At present, two fully working strings of the ARCA detector are in data taking, while the first string of ORCA will be deployed before mid 2017. The growth rate of KM3NeT detectors is mostly constrained by the funding. The total cost after the Phase-3 is foresaw to be between 220 and 250 million Euros. The funds for Phase-1 are secured.



Figure 3.2: A KM3NeT DOM. See the text for description.

3.1 The Detection Unit

As already stated above, the Detector Units (DU) are vertical structures, also called *strings*, hosting 18 DOMs. In the ARCA configuration, each string is 700 m high and the average horizontal spacing between detection strings is about 95 m. Even though each DOM contributes with its own buoyancy, a buoy system attached on the top of the string is needed. The DU is anchored to the seabed by a steel structure that hosts the DU-base. Here, an FPGA-based board, similar to that described in section 3.2, together with a DWDM¹-based system is responsible for the communication between the DOMs and the shore-station. The DU base also hosts the following components:

- a piezo-electric acoustic sensor;
- an hydrophone, similar to that used in the NEMO project;
- a *laser-beacon*, a device controlled from the shore, that produces a light beam intense enough to illuminate the highest DOM, for time calibration purposes;

¹The *Dense Wavelength Division Multiplexing* allows coexistence of multiple data channels on a single optical fibre pair by dedicating a wavelength to each channel.

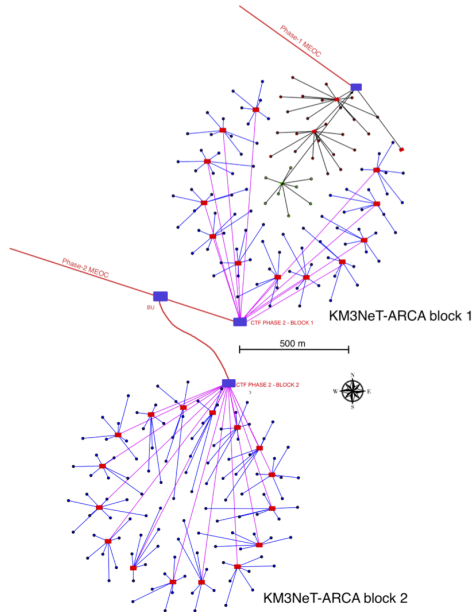


Figure 3.3: Footprint of the Phase-2 ARCA detector, made of two building blocks. The blue dots represent the strings, the blue lines represent the electro-optical cables that connect strings with the *junction boxes* (JBs, red squares), the pink lines connect the JBs with a *cable termination frame* (CTF, blue rectangles), in turn connected to the shore through the red *main electro optical cables* (MEOCs).

- an *acoustic beacon* that allows continuous positioning of the DOMs, repeatedly emitting a characteristic acoustic signal.

A prototype Detection Unit hosting 3 DOMs operated successfully since its deployment in the Capo Passero site in May 2014 until its decommissioning in July 2015 [72]. It validated the DU structure at the depth of 3500 m providing a test bench for the operation and data handling tools. The prototype allowed for long-term monitoring of the optical background, improving the knowledge of the marine site.

3.2 The Digital Optical Module

The digital optical module is one of the main innovation introduced by KM3NeT. In forerunner experiments, the electronic components were mostly decoupled with respect to the sensors, being placed in a dedicated container outside the optical module. The KM3NeT DOM itself hosts all front-end and power conversion boards together with sensors. In particular, it contains:

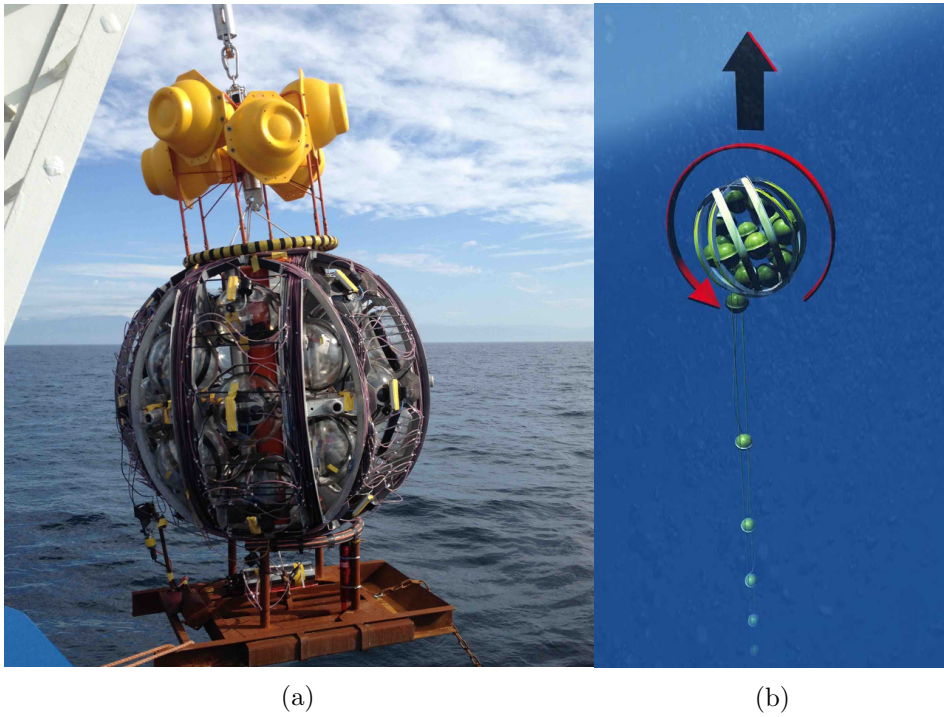


Figure 3.4: Picture of a furling DU being dipped in water (3.4a) and the principle of the launch vehicle unfurling (3.4b) [67]. During the transportation and the first phases of the deployment the strings are hosted furling in a *Launching vehicle of Optical Modules* (LOM). Once connected to the sea floor cabling infrastructure, the LOM releases the string during the unfurling.

- 31 3" PMTs and their specific power feeding electronics;
- a piezo-electric acoustic sensor glued at the internal bottom of the glass sphere;
- an *attitude and heading reference system* (AHRS) that provides 3-axis gyroscope, accelerometer and magnetometer;
- read-out, synchronisation and digitising electronics implemented onto a FPGA-based system, called *central logic board* (CLB);
- a *nano-beacon*, a LED sited in the top hemisphere of each DOM which can illuminate the optical modules vertically above for calibration purposes;
- power equipment, named *power board* (PB);
- optics and networking subsystems.

Indeed, each DOM is capable of standard Ethernet connectivity and is connected to a computer network implemented over fibre optics that extends from shore to the whole underwater detector. Most of the PMTs, 19 out of 31, are placed in the so-called *southern hemisphere*, i.e. the halve that occupies the lowest position, while the last 12 are placed in the *northern hemisphere*. The connection cables and the heat sink are placed at the top of the DOM (see figure 3.2 and figure 3.5). This reduces the sensitivity to downward-going light with respect to that of the upward-going one.

Each photomultiplier charge signal is sampled by a fast analogue-to-digital converter (ADC) with nanoseconds resolution (1 GHz). If the signal exceeds a certain threshold, the time spent over this threshold is then counted. This time duration is called *time over threshold* or *ToT*. A photon *hit* is defined by the ToT and its time of occurrence. A hit is generally related to a photon "hitting" the photo-cathode surface of the PMT. The threshold is set to a fraction of the typical electric charge due to a photon, typically one third or one quarter. Spurious signals can exceed the threshold and for this reason, hits whose ToT is less than 2 nanoseconds are discarded. The hits revealed by all the PMTs of a DOM are collected by the Central Logic Board (CLB), which subdivides them into *time frames* (TF). A TF is the collection of all hits occurring within a certain time window, typically set to 100 milliseconds. The frames are sent to the on-shore data acquisition system. Details about the on-line computing are discussed in chapter 4.

All the DOMs are time synchronised using a common time reference, distributed by a GPS receiver placed at the on-shore station. All CLBs use this shared global clock to build the time frames in phase with respect to each other and to the round of the GPS time, allowing the reconstruction of the status of the detector at the nanosecond level.

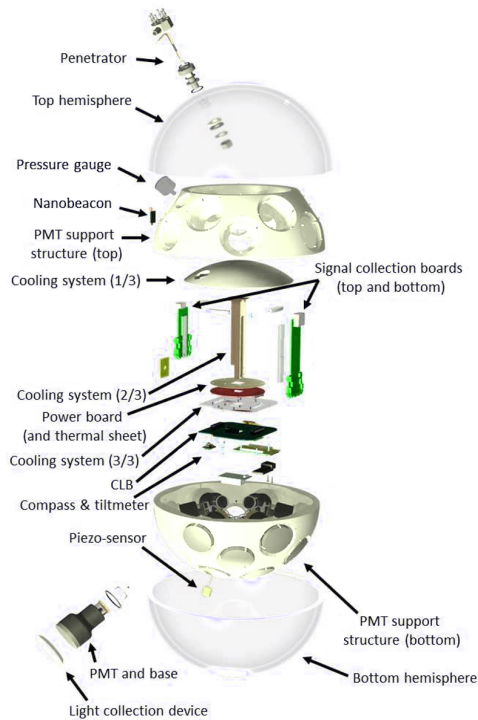


Figure 3.5: Breakout image of a DOM.

3.3 Background sources

3.3.1 Optical background

The presence of the potassium-40 radioactive isotope in sea water represents the most important continuous optical background source. The ^{40}K undergoes the three types of β -decay:



The maximum energy released to the electron, in the most significant decay mode (3.1), is about 1.33 MeV, well above the threshold for the Čerenkov effect, and the light emitted by these β -rays can simulate the Čerenkov signal from muon or cascade event on a PMT. The effect, in terms of photons detected by the the KM3NeT PMTs, is a continuous poissonianly distributed hit rate between 6 and 7 kHz [73].

This random and uncorrelated background is largely rejected by means of simple, yet powerful, trigger algorithms that are discussed in chapter 4.

Another source of optical noise is represented by the so-called *dark current*. Between the dynodes of a PMT high voltages are present (100 ÷ 1000 V) and due to the thermoionic effect electrons can be produced and amplified without the presence of any light. The dark current of the PMTs used by KM3NeT contributes to the hit rate with about 1 kHz at a temperature of 25 °C [74].

A further source of optical signal is present in sea water: a number of species, from bacteria to crustaceans and fishes living in the abyssal environment. These biological forms produce light for various reasons, like reproduction and predation [75]. This light can sporadically be revealed by the neutrino detectors as an enormous increase in the hit rates, up to some 10 MHz [73]. Such light emission is referred to *bioluminescence phenomena*.

3.3.2 Atmospheric muons and neutrinos

The most abundant signal in a neutrino telescope is given by atmospheric muon bundles produced by the decay of short-lived particles in CR extensive air showers. High-energy muons are highly penetrating particles and can reach the detector even if it is hidden behind several kilometres of shielding material. When these penetrating muons are above the Čerenkov threshold, their light can be detected by the optical sensors. In order to remove this huge background, a geometrical selection is applied. The atmospheric muons can only be downward-going tracks while upward-going ones are due to the neutrino-induced muons only, since neutrinos are the only particles that can traverse the Earth. Indeed, already at ~ 14 km water equivalent, all atmospheric muons are absorbed or decay and muon tracks are only induced by neutrinos (see figure 2.12). For this reason, the search for neutrinos is mainly done by looking downward.

Nevertheless, the Čerenkov radiation produced by atmospheric muon bundles induces signals on the PMTs that the reconstruction algorithms can reconstruct as fake upward-going particles. The strategies to reject this background of wrongly reconstructed atmospheric muons from neutrino induced muons have been defined and tested in every neutrino telescope.

An irreducible background for the observation of cosmic neutrinos is given by atmospheric neutrinos produced by the decays of short-lived particles (mainly muons, pions, and kaons) in the atmospheric showers. The energy spectrum of these atmospheric neutrinos is, asymptotically, a power-law steeper than that of the cosmic rays. The cosmic neutrinos, that are produced at the CR acceleration sites, are expected to follow the same power-law spectrum as the primary particles at the source. The energy spectrum of primary CRs at the top of the atmosphere is steeper than that expected at the acceleration sites because of the propagation of primaries in the galaxy. Cosmic neutrinos can be differentiated from atmospheric neutrinos by an energy estimation. Above 100 TeV (20 TeV), cosmic muon (electron) neutrinos

are expected to be more abundant than the atmospheric component. The atmospheric background due to tau neutrinos can be considered negligible, apart from small effects at low energies due to the oscillation of atmospheric ν_μ and a possible prompt component at extremely high energies.

3.4 Networking infrastructure

Another element of innovation with respect to the previous neutrino telescopes is represented by the network system developed by KM3NeT. It is implemented by means of a switch fabric based on fibre optic connections between the on-shore station and the DOMs, off-shore.

The on-shore switching infrastructure is composed of a network of White Rabbit (WR) [76] devices. The WR is an Ethernet-based technology which ensures both sub-nanosecond timing propagation and deterministic data transfer integrating Precision Time Protocol (PTP) [77] and Synchronous Ethernet (Sync-E). It uses the master-slave paradigm to provide sub-nanosecond timing accuracy between WR compliant devices. In the master-slave relationship, the master provides a clock with picoseconds precision to all the slave devices connected to it, letting them to synchronise and syntonise² their local clocks with the one of the master.

The main peculiarity of the KM3Net network distribution is its physical topology. Every single DOM has a unidirectional 1 Gbps³ uplink to reach the on-shore station that allows to transfer the acquired data. On the other side, the on-shore station has a unique unidirectional 1 Gbps downlink to reach all the DOMs, so-called *slow control* (SC) link. It allows to drive the DOMs through the required configuration steps and to receive periodic information about the DOM health and status. The SC is shared by every single DOM so that a packet addressed to one DOM is also received by all the others. A software running on the DOM's FPGA ignores all packets not addressed to it. This topology highly reduces the communication resources cost at this facility, but it requires customising the communication elements as the switches and nodes – DOMs and on-shore computers. A deep customisation of WR switch at software level has been done transforming it from a synchronisation point-to-point technology with bidirectional links between two devices to a synchronisation device for the DOMs by asymmetric and unidirectional links. This customisation allows sharing one unidirectional downlink among 360 DOMs, highly optimising the communication resources.

Synchronous data transfer also allows to determine precisely the latency given by the data transport layer, which, in the case of KM3NeT, has been measured to be less than 1 ms.

²Two clocks are *syntonised* if they change their counters at the same time; they are *synchronised* if the values of the counters coincide.

³ 2^{30} bits per second.

Chapter 4

Trigger and Data Acquisition System for KM3NeT

4.1 TriDAS design

The *Trigger and Data Acquisition System* (TriDAS) is a computing system devoted to the read-out, aggregation and filtering of the continuous data flow from the KM3NeT detector, taking care of storing of interesting portions of data in the form of *triggered events*

Due to the high optical background caused by β -processes of ^{40}K and the bioluminescence phenomena in sea water, an on-line trigger system is required. Indeed, storing the corresponding throughput would not be a sustainable solution. As for the ANTARES and NEMO projects, in order to minimise the complexity of the underwater electronics, no off-shore hardware trigger is implemented and the all-data-to-shore approach is used: all detected optical signals are sent to shore via a computer network that includes the shore-station and the detector. Moreover, this approach eases system upgrades, made possible by the future technologies that are foreseen by the Moore's law¹ [78]. The expected data throughput from the Phase-2 (see table 3.1) ARCA detector is between 50 and 250 Gbps, depending on the background hit rate per PMT.

4.1.1 On-line software

TriDAS contains several software packages working together to allow the control and the monitoring of the system.

¹“*The complexity for minimum component costs has increased at a rate of roughly a factor of two per year. Certainly over the short term this rate can be expected to continue, if not to increase. Over the longer term, the rate of increase is a bit more uncertain, although there is no reason to believe it will not remain nearly constant for at least 10 years.*”. Despite the initial prevision, the Moore's law is still valid in 2017, with some generalisation.

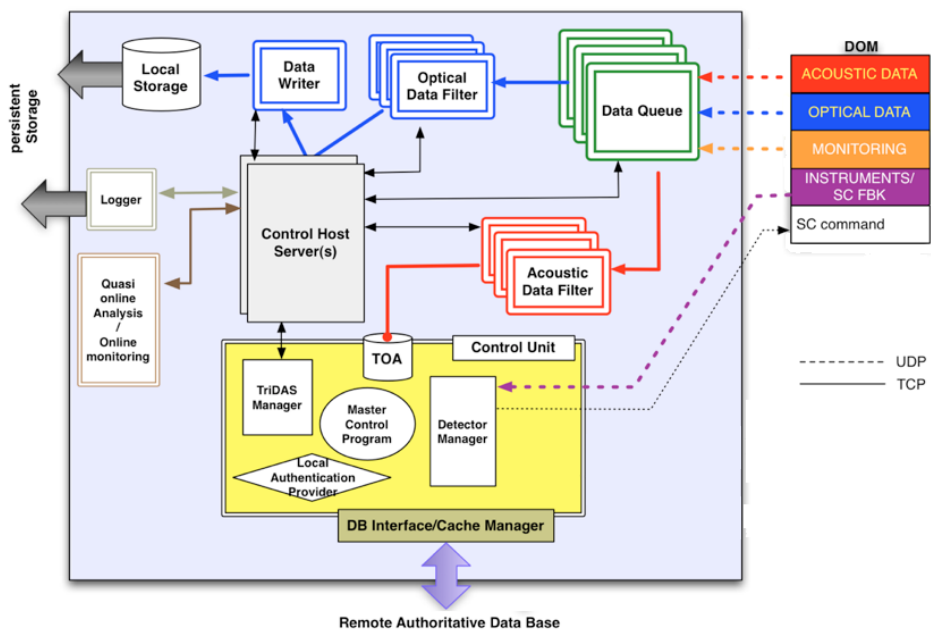


Figure 4.1: Sketch of TriDAS. Dashed or solid lines refer to data links implemented over UDP or TCP protocol, respectively. Colours correspond to different data flows: acoustic data (red), optical data (blue), monitoring data (orange), serial instruments data and Slow Control feedback (purple), and white (SC commands).

The following sub-components can be identified:

- *TriDAS Core* is the *mission critical* part of the package, i.e. the set of programs in charge of the data acquisition. The Core programs must provide the maximum duty cycle. The overwhelming majority of the computational power is allocated by the Core programs.
- the *Control Unit* is the set of programs that allows to steer both the TriDAS core applications and the off-shore detector;
- the *Quasi-on-line Analysis and Monitoring* (QOLAM) suite of programs provides summary graphical visualisation of the status of the detector.

TriDAS Core

TriDAS Core applications are devoted to the collection, filtering, and storing of the detector data. The first data processing stage is represented by the *DataQueue*² (DQ). The program is in charge for the aggregation of unfiltered optical and acoustic data and of their distribution to the computers dedicated to the on-line analysis and trigger, namely *DataFilters* (DFs). For each of the two data streams, a specific implementation of the DF exists: the *acoustic DataFilter* (aDF) and the *optical DataFilter* (oDF). Each DQ is responsible for the collection of data coming from a *sector* of the detector and is topologically connected to a subset of DOMs. Due to the limited capabilities of the FPGA in the DOM, each time frame is divided into a number of UDP datagrams³, that asynchronously reach the DQs through the network.

Each aDF receives all data from a single DQ continuously, thus having the complete data time series from a subset of the acoustic sensors. The aim of the aDF is the on-line reconstruction of the *time of arrival* of the acoustic signals emitted by the beacons of the positioning system [62]. The output of all the aDFs is collected by the *Data Base Interface* (DBI, see below) and written in the main database of the experiment. In the following part of this section, the focus will be on the optical data only, as the acoustic part is not directly involved in the present study. Details on the acoustic data processing can be found in [62].

²Although it is not part of this thesis, the design and implementation of the DataQueue, together with other “satellite” applications developed for debug purposes, have been an important part of the work done during the last three years.

³The *User Datagram Protocol* (UDP) is one of the core members of the Internet Protocol (IP) suite. The UDP uses a simple connectionless transmission model with a minimum of protocol mechanism in order to minimise the transmission overhead. The lack of a connection protocol, in contrast to what happens with the *Transmission Control Protocol* (TCP), makes the end-points unaware of the delivery of messages. The packet loss detection is thus demanded at the user level.

Each oDF receives a bunch of data belonging to a time interval, called Time Slice (TS) from all the DQs. A full TS contains a snapshot of the whole detector. The TS duration is a constant defined for each run, typically set to 100 ms. The TS is assigned to an oDF according to the time stamp of the TS itself, selecting the next from a fair round-robin.

Section 4.2 contains more details about the trigger system implemented by the oDF program.

Triggered data coming out from the oDFs are sent to the *DataWriter* (DW) that collects them on permanent storage in ROOT [79] format. A server program implementing the *ControlHost* (CH) [80] protocol is used for triggered data transmission. The program allows dispatching of generic data with a *publish-subscribe* paradigm in *multiple-input and multiple-output* (MIMO) mode. Multiple clients can *publish* a datum to a *tag* – a data channel – while other clients can receive it by *subscribing* the tag.

The usage of the CH allows all oDFs to publish to a dedicated tag without caring about the subscribers. As a consequence, the oDFs and the DW do not have to keep many connections alive. This greatly simplifies the programs allowing optimisation of the resources of the computing elements devoted to the trigger.

The ANTS system, described in chapter 5, benefits of the ControlHost dispatcher, thus does not interfere with the TriDAS Core processes.

Time delays

The time delay between the detection of a neutrino event and the follow-up measurements is a critical parameter. In the following it will be referred to as *transit time*. A detailed characterization of all elements must be performed, in order to determine the potential of the multi-messenger study.

The time spent by the signals in the DOM and in the network, as reported in section 3.4, is generally negligible with respect to the computing time. Optical to electric signal conversion time by a typical KM3NeT PMT and sampling time are of the order of few tens of nanoseconds. Time delay due to the transmission of data over optical fibre is of the order of one millisecond.

From the point of view of the timing of data, the DQs act as a delay – a *buffer*, in jargon – that can be tuned by the user by changing the timeslice duration. Data going through a DQ are fairly queued, i.e. the transmission strictly adhere to the *first in-first out* (FIFO) paradigm. The value of the delay is set to 5 times the TS duration, thus typically 500 ms. The number of optical time frames is not known in advance since it is proportional to the number of hits recorded by the DOM. In particular, the number of UDP

fragments is roughly⁴ given by:

$$N_{UDP} \approx \text{ceil} \left[\frac{N_{hits} \cdot \text{sizeof}(\text{hit})}{M} \right] = \text{ceil} \left[\frac{R_h \cdot \Delta_{TS} \cdot \text{sizeof}(\text{hit})}{M} \right] \quad (4.1)$$

where N_{hits} and R_h are the number of hits and the hit rate, respectively, Δ_{TS} is the duration of the timeslice, $\text{sizeof}(\text{hit}) = 6$ Bytes, M is the maximum transfer unit (MTU) set by the network, typically 9000 Bytes, and the ceil function returns the smallest integral value not less than its argument. This fixed delay is introduced to allow safely retrieving all datagrams belonging to a Time Frame (TF) before the reassembling and transmission to the proper DataFilter.

In order to avoid halting of the system in case some DOMs or DQs are missing, also the oDF implements a time-out based mechanism for assembling the Time Slice from the various TFs. The condition to start the trigger algorithms is the first occurrence between the completion of the data sets from all known DOMs and the expiration of a timer, that is set at the first TF arrival time. The timer's delay is set to 1 second.

Hereafter, the time contribution given by the ANTS system, described in subsection 6.2.4, must be added to the transit time.

Control Unit

The Control Unit (CU) [81], which represents the user interface to the detector, aims at coordinating the TriDAS and operating the DOMs through a dedicated SlowControl (SC) protocol. It is composed of the following sub-systems:

- *Master Control Program* (MCP): the main user interface and allows to schedule the data taking of the experiment;
- *Local Authentication Provider* (LAP): provides a unique place to define the list of services, the local user accesses and the network configuration;
- *TriDAS Manager* (TM): steers the on-shore computing facility, setting up the TriDAS processes, realising the run-setup defined by the MCP;
- *TriDAS Manager Agent* (TMA): acts as a local proxy to start, stop and monitor the TriDAS core processes on a server machine;
- *Detector Manager* (DM): controls and configures the off-shore detector, implementing the run-setup defined by the MCP;

⁴In each datagram, two parts are recognised, a *header* part, written at the beginning, and a *payload*, found right after the header. The first part contains important information for identifying the DOM, its status, and the coarse time stamp. The payload is essentially filled with an array of hits up to the end of the datagram. The size of the datagram is thus given by the sum of its parts, the first being typically negligible with respect to the second.

- *Data Base Interface* (DBI): provides local database caching and synchronisation with the main remote DB [82] of the experiment;

All of the CU programs, except the TMA, run together on the same computer. The TMA runs on the same server where a TriDAS core application is meant to run.

QOLAM

The Quasi On-Line Analysis and Monitoring [83] is a suite of programs that performs fast analyses on a subset of the collected post-trigger data, and visualisation and monitoring. It is composed by:

- ROyWeb, a web-based program allowing the representation of monitored parameters as time series, histograms or synoptic plots;
- Rainbow Alga, a 3D event display;
- ROyFit, a fast muon reconstruction software, based on an algorithm used in the ANTARES experiment [84].

4.2 Trigger system

The oDF is the central core of the trigger facilities of TriDAS. Two different levels of filters are implemented: the *Level 1* (L1) filters apply very simple conditions, mainly devoted to reject as many uncorrelated background signals as possible; the *Level 2* (L2) algorithms validate the events selected by the L1, using more complex topological and temporal conditions.

Uncalibrated⁵ unfiltered hits – as they are created by the DOMs – are usually referred to as *Level 0* (L0) hits. Every L0 hit that satisfies one of the L1 trigger conditions is marked as a *triggered hit* (TH), and a *triggered event* (TE) is built around it with the hits occurred in a customisable time window, typically $\pm 3 \mu s$. If more TEs overlap, they are merged within an extended time window. The non-triggered hits contained in a TE are referred to as *snapshot hits*. The Triggered and snapshot hits together are generally referred to as the *L1 hits*.

The L1 filters are:

- *simple coincidence* (SC): one or more hits on different PMTs in the same DOM within a coincidence window of 5 ns;
- *charge excess* (Qtrig): hits whose time over threshold exceeds that corresponding to a signal due to three photo-electrons.

⁵The position of each DOM is determined on-line by by means of the acoustic positioning system. PMT orientation is derived by the data coming from the AHRS.

In the following subsections, a description of the L2 filters is presented. These algorithms, based on the output of the L1s, aim at studying events of various topologies.

4.2.1 T-Triggers

Three T-Triggers, named T1, T2 and T3, are defined considering coincidence conditions between L1 hits. The T1 condition is satisfied when two L1 hits occur on the same DOM within a coincidence window of 55 ns. The T2 requires two L1 hits occurring on adjacent DOMs of the same DU within a time window of 200 ns. The T3 is satisfied when at least two L1 hits occur in adjacent and next-to-adjacent DOMs of the same DU in 200 ns.

4.2.2 Simple Causality filter

The Simple Causality filter searches for coincidences of a predefined number of L1 hits within a time window defined according to the distance between the involved PMTs. Moreover, the trigger seeds must obey the following causality condition:

$$|t_i - t_j| \leq |\vec{r}_i - \vec{r}_j| \frac{n}{c} \quad (4.2)$$

where t_i is the time of the i -th hit, \vec{r}_i is the position of the hit PMT and c/n is the group speed of light in water.

4.2.3 Sky Scan trigger

As for the Simple Causality filter, the Sky Scan trigger is applied only if the number of L1 hits within a time window, determined by the position of the involved PMTs, is greater than a certain threshold. A predefined number of isotropically distributed directions is initially generated. For each of them, the detector is rotated and the z -axis is aligned to the chosen direction. The following condition is then tested:

$$|(t_i - t_j)c - (z_i - z_j)| \leq \tan \theta_c \sqrt{(x_i - x_j)^2 + (y_i - y_j)^2} \quad (4.3)$$

where θ_c is the Čerenkov angle in water. If the number of L1 hits satisfying equation 4.3 is greater than a predefined threshold, the event is validated.

4.2.4 Tracking trigger

The Tracking trigger is derived from the Sky Scan trigger. Instead of doing a survey of the whole sky, the directions are obtained calculating the position of a set of interesting astrophysical objects at the time of data acquisition. The detector is then rotated as in the Sky Scan trigger and the

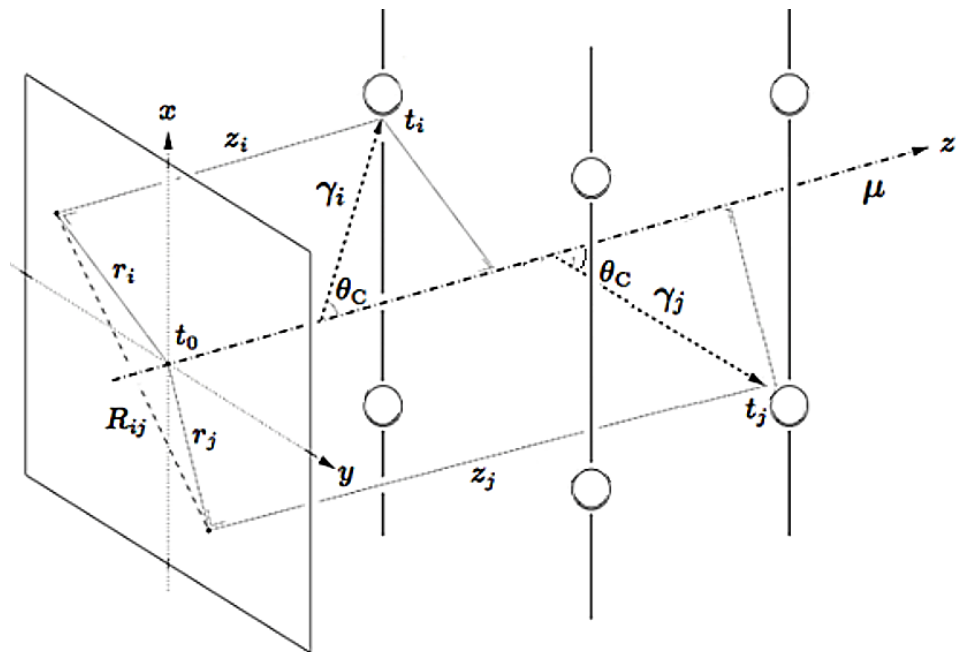


Figure 4.2: Schematic view of a track event. The z -axis of the detector is rotated to match with the direction of propagation of the muon. All important quantities are highlighted. Refer to the text in subsection 4.2.3 for the description.

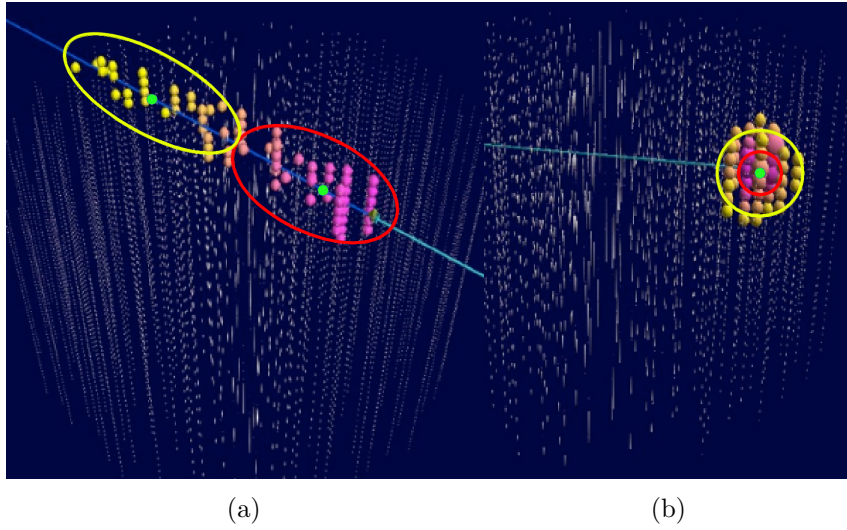


Figure 4.3: Track (4.3a) and shower (4.3b) Monte Carlo events shown using the KM3NeT event display. The event is divided into two temporally disjoint parts. The coloured circles and the green dots had been superimposed in order to represent the groups of hits and the centres of mass, respectively. The colour of both hits and circles represents the time, growing from red to yellow.

condition in equation 4.3 is used. The trigger is satisfied when the surface density of the hits in the plane orthogonal to the considered direction exceeds a predefined threshold.

4.2.5 Vertex Splitting trigger

The Vertex Splitting trigger allows to discriminate between spherical- and track-shaped events, corresponding to cascade and muon events, respectively. The hits of each event are divided in two groups, according to their time of occurrence. The geometrical centre for each group is then calculated. Finally, the inertia tensor is computed as:

$$I^{j,k} = \sum_i A_i \left(\delta^{j,k} r_i^2 - r_i^j \cdot r_i^k \right) \quad (4.4)$$

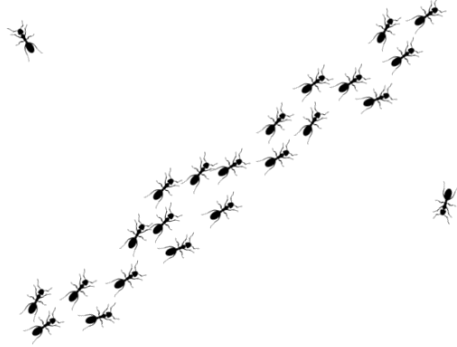
where $k, j = x, y, z$, \vec{r}_i and A_i are the positions with respect to the geometrical centre and the number of hits of the i -th DOM, respectively. To determine the shape of the event, the ratio between the minimum of the eigenvalues of the inertia tensor and their sum is calculated:

$$T = \frac{\min(I_1, I_2, I_3)}{I_1 + I_2 + I_3} \quad (4.5)$$

If $T \approx 1/3$ the event is considered spherical as there is no leading direction, while if $T \approx 1$ the event is classified as track-like.

4.2.6 External trigger

An external trigger is set when an alert message from another experiment, such as a GRB event detected by a satellite, is received. When it occurs, each DF writes to file all L0 hits recorded in the last minutes, making them available for further off-line analysis. The required data buffer is constrained by the data rate and by the time needed to deliver the alert through the Internet, typically few minutes. This system is the multi-messenger complementary to the ANTS system, discussed in chapter 5 and chapter 6.



Chapter 5

ANTS: Astrophysical Neutrino Trigger System

5.1 Multi-messenger astronomy

Multi-messenger astronomy is the combination of observations in cosmic rays, neutrinos, photons of all wavelengths and gravitational waves. It represents a powerful tool to study the physical processes driving the *non-thermal* Universe. Neutrinos play an important role in this emerging field.

The detection of a diffuse flux of astrophysical neutrinos by IceCube [59, 85] with no clearly resolved sources further motivates a multi-messenger approach. The observation of astrophysical neutrinos can provide critical directional information that can be used to guide follow-up observations. Additionally, the detection of a neutrino source is a strong signature of high-energy hadronic interactions. This feature could shed light on the accelerating mechanisms which produce the most energetic particles observed in the Universe.

Several models predict neutrino emission from flaring objects or other transient phenomena, such as gamma-ray bursts [86], core-collapse supernovae [87], or active galactic nuclei [88].

Multi-messenger research programs offer a unique opportunity to detect transient sources. By combining information provided by the KM3NeT neutrino telescope with that coming from other observatories, the probability of detecting a source is enhanced, allowing the possibility of identifying a neutrino progenitor from a single detected event. A rapid start of follow-up is required to enhance the possibility of successful observations.

In this chapter, the ANTS system is described, while its performances are reported in chapter 6.

5.2 Description of the system

ANTS is a software that aims to perform an on-line – possibly real-time¹ – fast reconstruction of neutrino track events recorded by the KM3NeT detector, and to send alert neutrino messages when a predefined condition is satisfied.

The program is composed by two main sub-parts:

- the *reconstruction units* (RUs) are elements working in parallel to reconstruct tracks from L1 events triggered by the optical Data Filters;
- the *trigger unit* (TU) is the component that, starting from the output of the reconstruction units, takes the decision whether to send an alert message.

Term	Definition
L0 hit	not calibrated information about the time of occurrence, the time over threshold and the channel id of a PMT signal exceeding a predefined threshold, typically related to the detection of a photon on the PMT
Time Slice (TS)	collection of L0 hits occurring in the whole detector within a precise time window, typically of 100 ms
DataFilter (DF)	computing element of the DAQ system devoted to the on-line trigger. It produces L1 Events starting from the L0 hits in a Time Slice
Triggered hit	L0 hit satisfying at least one trigger condition
Snapshot hit	L0 hit not satisfying any trigger condition but belonging to a L1 Event
L1 Event	collection of hits (triggered + snapshot) occurring within a time window of about $5.5 \mu\text{s}$, centred around the first triggered hit
L1 hit	hit belonging to a L1 Event (either triggered or snapshot)

Table 5.1: DAQ common terms.

¹The time spent by a program or procedure that is meant to be executed *on-line* is constrained *on average*, i.e. the program has to complete a certain number of tasks within a certain cumulative amount of time. A *real-time* program must complete *any* of its tasks within fixed amount of time, i.e. the time spent in worst case is constrained.

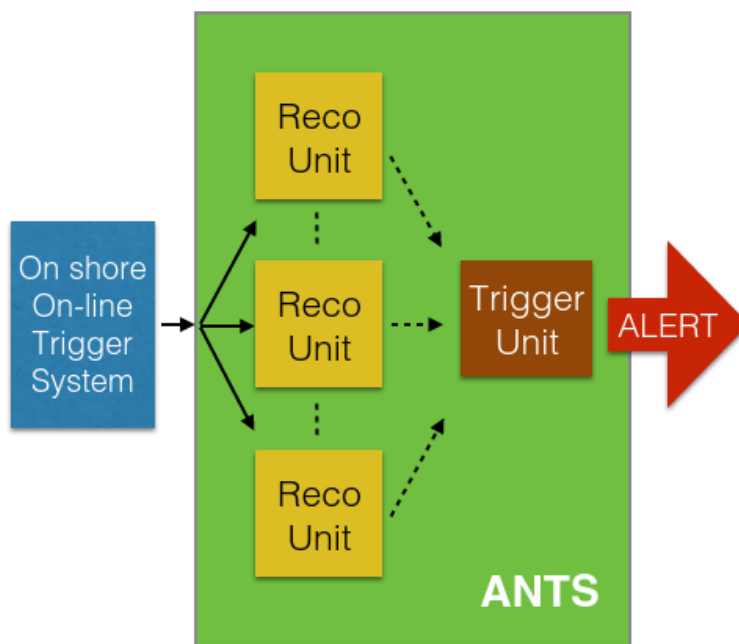


Figure 5.1: Block-diagram view of ANTS. Solid lines indicate the triggered events data flow, logically directly connecting the on-line trigger system, i.e. the oDFs, and one of the reconstruction units (yellow boxes). Dashed lines represent reconstructed tracks flow. A single trigger unit (brown box) decides whether to send an alert message or not basing on the output of a set of selection algorithms it implements.

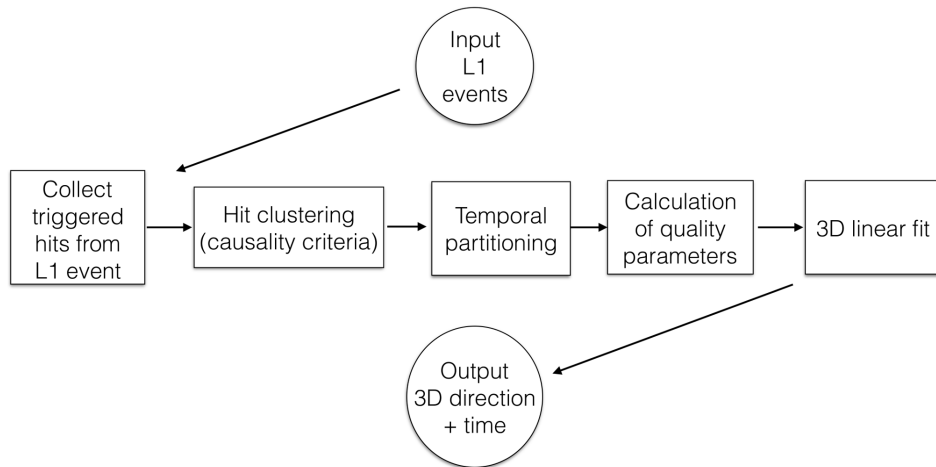


Figure 5.2: Simplified flow chart of the reconstruction algorithm. No-output exit points are not shown. See the text for a description.

5.2.1 Reconstruction algorithm

The track reconstruction algorithm represents the most complex and time consuming part of ANTS. As it deals with all of the information provided by the on-line filtering system, it needs more resources than the rest of the system. Several reconstruction units work in parallel in order to distribute the work load and optimise the alerting time. Each RU, which is an identical copy of the same procedure described hereafter, takes care of a triggered event at a time.

For reference, table 5.1 recalls the meaning of several terms that were introduced in chapter 4.

The reconstruction procedure is organised in the following **steps**, as shown in figure 5.2. For each L1 event produced by the optical DataFilters, only triggered hits are considered and time ordered. The snapshot hits are ignored. On the contrary, the off-line reconstruction algorithms typically consider all the hits.

A hit **clustering** based on causality criteria is performed. A **temporal partitioning** algorithm is applied to each recognised cluster. The *centroid* of each temporal partition element is calculated. A centroid is the centre of mass and average time of the triggered hits occurring in the partition element.

A partition element counting less than 10 triggered hits is ignored by the procedure. A minimum number of 3 centroids in the cluster is required for a sensible result, so clusters with 1 or 2 centroids are discarded. These two conditions define the ANTS' *minimum requirements* for starting the processing.

A quality parameter, that provides indication about how well the centroids

represent a straight-line, is defined and, if it exceeds a predefined threshold, a **linear fit** procedure over centroids is performed.

In the following sections, each of the above mentioned steps is discussed, in more details.

Clustering

The clustering procedure aims to produce subsets of hits that are more likely to be caused by the Čerenkov emission from the same relativistic particle moving in water. Given the expected muon rate $r \sim 100$ Hz in a km^3 detector, the probability of a *pile-up* event, i.e. an event with multiple muons arriving together within the event time window, is given by the Poisson distribution:

$$P(k > 1 \text{ in } \Delta T) = \sum_{k=2}^{\infty} \frac{\lambda^k \cdot e^{-\lambda}}{k!} = 1 - P(1) - P(0) = 1 - e^{-\lambda}(1 + \lambda) \approx 3.8 \cdot 10^{-8} \quad (5.1)$$

where $\Delta T = 2.75 \mu\text{s}$ is the half duration of a typical DAQ event and $\lambda = r \cdot \Delta T$ is the expected number of muons in such a time interval. While a pile-up event is quite unlikely to occur, clustering allows filtering the spurious coincidences due to ^{40}K decay and bioluminescence phenomena.

The algorithm exploits a space-time condition between two hits, called *affinity*, is defined as:

$$\text{affinity} = \begin{cases} |\Delta t| \cdot v_g \leq d & \text{if } d \neq 0 \\ |\Delta t| \leq 20 \text{ ns} & \text{if } d = 0 \end{cases} \quad (5.2)$$

where Δt is the time elapsed between the two hits, v_g is the group velocity of light in water, about 0.2171 m/ns [89], and d is the distance between the two DOMs.

At the beginning of the procedure, the first triggered hit is assigned to a new cluster. This is done also in case a triggered hit is not affine to any cluster. Then, the affinity of each triggered hit in the event is tested against the last hit of each cluster and if the condition is satisfied for only one cluster, the hit is added to it. If more than one cluster satisfies the condition, then for each of them a score is calculated as the size of the longest sequence of consecutive hits that are affine to the testing hit. The hit is assigned to the cluster with the highest score.

Temporal partitioning

The temporal partitioning procedure creates a set of temporally disjoint subsets of the triggered hits in a cluster. Each subset has a fixed time

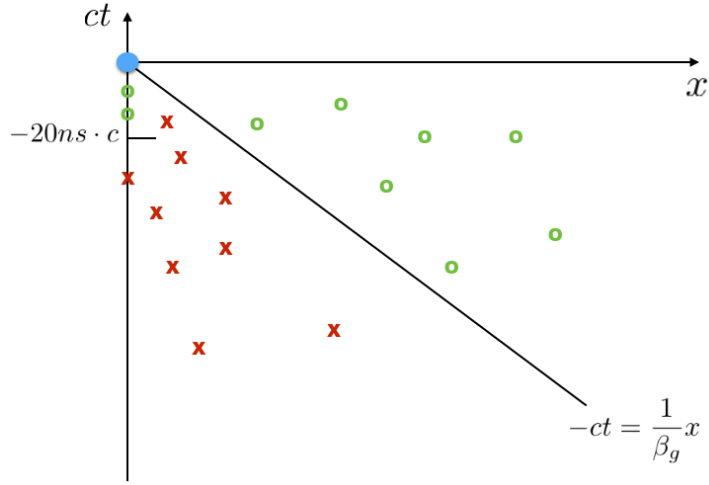


Figure 5.3: Space-time diagram with a testing hit (blue circle, in the origin) and other hits. Red crosses and green circles represent hits not satisfying and satisfying the affinity condition in equation 5.2, respectively.

duration that is calculated as a fraction of the *inter-quartile range* of the hit time distribution:

$$\Delta T = \frac{1}{K}(Q_3 - Q_1) \quad (5.3)$$

i.e. one k -th, typically $\frac{1}{5}$, of the time between the first and the third quartiles of the cluster hit time distribution (see figure 5.4). Assuming that the bulk of the triggered hits is provided by a high-energy muon, this partitioning approach allows to concentrate the bulk of the hits in the cluster into a reasonable number of partition elements. Spurious coincidences before and after the triggered hits due to the muon are easily isolated into separate partition elements. Indeed, elements containing less than ten triggered hits are ignored in following processing.

The centre of mass and average time of the hits in each “surviving” partition element make a *centroid*. Averaging the spatial coordinates and times of the hits in calculation of centroids allows to relieve the effects due to the scattering of light in water and the spread of light with respect to the muon trajectory caused by the Čerenkov effect. If the Čerenkov cone is well resolved, the centroid is very close to the trajectory of the muon.

Linear fitting

Given the application point $\bar{P}_0 = (x_0, y_0, z_0)$ and the vector $\vec{v} = (a, b, c)$, a straight-line in a 3D space is defined by the first three members in equa-

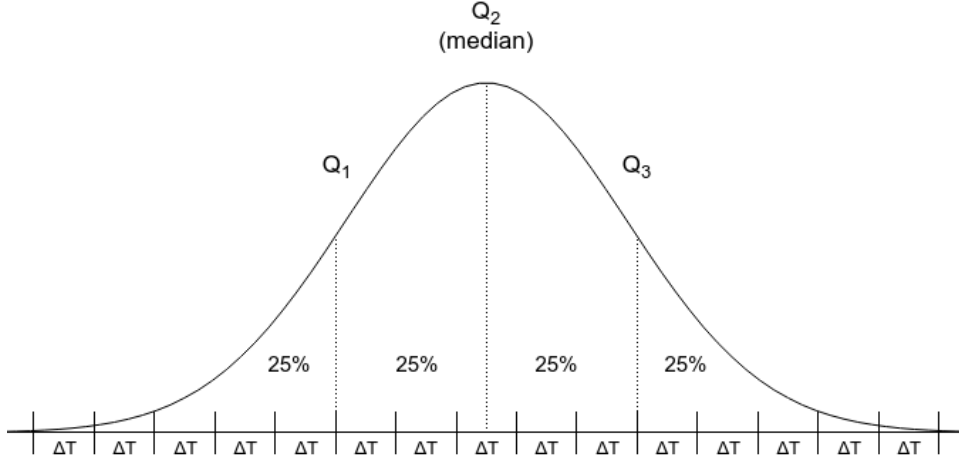


Figure 5.4: Example of temporal partitioning. The quartiles of a set of data values are the three points that divide the data set into four equal groups, each group comprising a quarter of the data. The second quartile (Q_2) is the median of the distribution. The time between the first (Q_1) and the third (Q_3) quartiles is divided into 5 equal intervals (ΔT), as defined in equation 5.3.

tion 5.4:

$$\frac{x - x_0}{a} = \frac{y - y_0}{b} = \frac{z - z_0}{c} = t \quad (5.4)$$

The parameter t , used to disentangle the line equation coordinates into the parametric linear system in equation 5.5, is given by the time associated with the centroid. In such a way, the vector \vec{v} defines a velocity that can be associated to the speed of the muon, that is opposite to the direction of the hypothetical source.

$$\begin{cases} x = a \cdot t + x_0 \\ y = b \cdot t + y_0 \\ z = c \cdot t + z_0 \end{cases} \quad (5.5)$$

Three linear weighted fits are performed, one for each equation in equation 5.5, over the selected centroids. The weights, one per spatial coordinate, associated to each centroid are given by:

$$w_\xi = N_{hits} \cdot \frac{g_\xi}{(D^2 + \sigma_\xi^2)} \quad (5.6)$$

where $\xi = (x, y, z)$ is the spatial coordinate, N_{hits} is the number of hits contributing to the centroid, $D = 0.2159$ m is the diameter of DOM and σ_ξ is

the root mean square of the ξ -coordinate of the hits. The g_ξ is a number that depends on the position of the centroid within the detector, and is defined as:

$$g_\xi(\bar{P}) = \begin{cases} 0.1 + 0.9 \cdot \frac{|P_\xi - \text{border}_\xi(\bar{P})|}{\lambda} & \text{if } |P_\xi - \text{border}_\xi(\bar{P})| < \lambda \\ 1 & \text{otherwise} \end{cases} \quad (5.7)$$

where $\lambda = 100$ m is about 2 times the blue light absorption length in water, $\text{border}_\xi(\bar{P})$ is the ξ coordinate of the detector's nearest border to the centroid \bar{P} .

The introduction of such a weight is motivated by the fact that a centroid whose position is far from the centre of the detector is also more likely to be far from the muon trajectory. Consider the slope of the curve reproducing one of the spatial coordinates versus the time of the centroids provided by a high-energy muon event that completely traverse the detector. In the central part, the curve would resemble a straight-line with the “correct” slope, while at the two ends it would flatten, with an approximately zero slope. This effect is due to the lack of hits outside the detector volume. Defining a *fiducial detector volume* would lead to a reduced detection efficiency, as all vertical tracks close to the border would be ignored. On the other hand, applying the weighted fit approach, centroids from vertical particles, close to the boundary of the active volume of the detector, would just be weighted in the same way, allowing the reconstruction. These “edge effects” will be taken into account later.

The linear least-square fitting method is used [90]. Till the end of the paragraph the $\langle [\cdot] \rangle = \sum_{i=1}^N w_i \cdot [\cdot] / \sum_{i=1}^N w_i$ operator is used to denote the weighted average, i.e.:

$$\langle x \rangle = \frac{\sum_{i=1}^N w_i \cdot x_i}{\sum_{i=1}^N w_i} \quad (5.8)$$

The equations to calculate the fit parameters, i.e. the \bar{P}_0 and \vec{v} components, are:

$$\Delta = \begin{vmatrix} \langle t^2 \rangle & \langle t \rangle \\ \langle t \rangle & 1 \end{vmatrix} \quad (5.9)$$

$$v_\xi = \frac{1}{\Delta} \begin{vmatrix} \langle \xi t \rangle & \langle t \rangle \\ \langle \xi \rangle & 1 \end{vmatrix} \quad (5.10)$$

$$P_{0\xi} = \frac{1}{\Delta} \begin{vmatrix} \langle t^2 \rangle & \langle \xi t \rangle \\ \langle t \rangle & \langle \xi \rangle \end{vmatrix} \quad (5.11)$$

Quality parameter

The definition of a quality estimator of the reconstruction result is a compelling item, mandatory to interpret its correctness.

The Pearson linear correlation coefficient gives an estimate of the linearity of the relationship between two variables [90]. Considering two variables, α and β , it is defined as:

$$R_{\alpha\beta} = \frac{\sigma_{\alpha\beta}}{\sqrt{\sigma_{\alpha}^2 \cdot \sigma_{\beta}^2}} \quad (5.12)$$

where $\sigma_{\alpha\beta}$ is the covariance of the two variables and σ_{α} and σ_{β} are their root mean squares.

Its value ranges between +1 and -1, where 1 corresponds to a total positive linear correlation, 0 to no linear correlation, and -1 to total negative linear correlation.

The first quality parameter is defined as:

$$q = |R_{xt} \cdot R_{yt} \cdot R_{zt}| \quad (5.13)$$

where x , y , and z are the spatial coordinates of the centroids and t is the corresponding time. The q ranges between 0 and 1, corresponding to bad match – at least of one of the 3 – and to perfect match, respectively. Both covariance and variances are weighted with the same weight defined in equation 5.6.

The q parameter is an estimator of the cluster quality, rather than of the reconstructed track. It does not rely on the fit result and can be calculated before starting the fit procedure.

Since the q parameter does not consider the number of degrees of freedom, it is used in association to its p-value, defined as:

$$p = 1 - (1 - p_x) \cdot (1 - p_y) \cdot (1 - p_z) \quad (5.14)$$

where p_{ξ} ($\xi = x, y, z$) are the p-values of the single Pearson's correlation coefficients:

$$p_{\xi} = ibeta \left(\frac{ndf}{2}, \frac{1}{2}, \frac{ndf}{ndf + \tau_{\xi}^2} \right) \quad (5.15)$$

where *ibeta* is the *incomplete beta function*, *ndf* is the number of degrees of freedom, i.e. the number of centroids - 2, and τ_{ξ} is the Student's t:

$$\tau_{\xi}^2 = R_{\xi t}^2 \cdot \frac{ndf}{1 - R_{\xi t}^2} \quad (5.16)$$

The p-value in equation 5.15 roughly indicates the probability of an uncorrelated system producing datasets with a Pearson correlation coefficient at least as extreme as the one computed from these datasets.

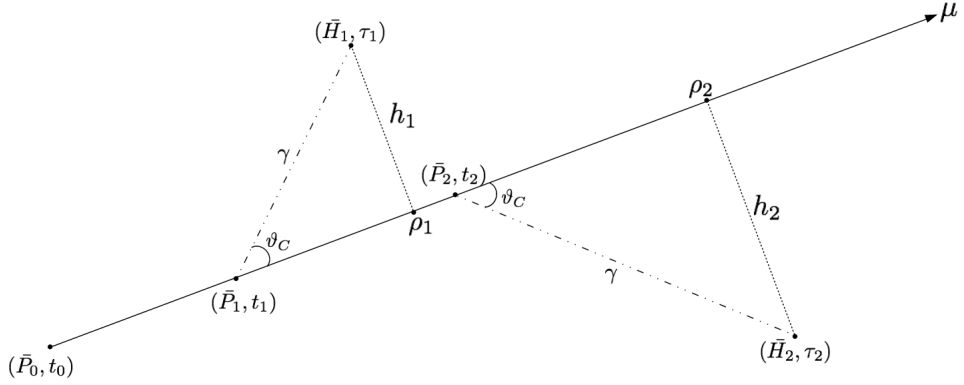


Figure 5.5: Schematic representation of the space-time relationship between a ultra-relativistic charged particle moving in sea water and the photon hits – the (\bar{H}_i, τ_i) pairs – revealed by the detector. See the text for a detailed descriptions of all terms.

An alternative quality parameter, that considers also the fit result, can be defined. Assuming that the reconstructed track corresponds to a high energy muon (μ) traversing the detector as shown in figure 5.5, the time τ_i of the i -th hit is given by:

$$\tau_i = \frac{d(\bar{H}_i, \bar{P}_i)}{v_g} + \frac{d(\bar{P}_0, \bar{P}_i)}{c} = \frac{1}{v_g} \frac{h_i}{\sin \vartheta_C} + \frac{1}{c} \left[d(\rho_i, \bar{P}_0) - \frac{h_i}{\tan \vartheta_C} \right] \quad (5.17)$$

where $d(\alpha, \beta)$ is the distance function, $\vartheta_C \approx 42^\circ$ is the Čerenkov light angle for an ultra-relativistic charged particle in water, ρ_i , $h_i = d(\bar{H}_i, \mu)$, and \bar{H}_i are the minimum approach point to the track, the distance from the track, and the position of the i -th hit, respectively. The \bar{P}_i and t_i are the light emission point and time of emission of the Čerenkov photon producing the i -th hit, respectively. The reconstruction parameters enter the equation in the \bar{P}_0 and ρ_i variables as $\bar{P}_0 = (x_0, y_0, z_0)$ is the starting point and ρ_i is a function of both \bar{P}_0 and $\vec{v} = (a, b, c)$.

The fraction of hits in the cluster that satisfy the causality condition with the reconstructed track through equation 5.17 can be used as an estimator of the goodness of the reconstruction. This procedure has been implemented into the ANTS code base but it is not used, since the quality parameters defined in equation 5.13 and equation 5.14 have been proven, with Monte Carlo studies shown in chapter 6, to be good quality estimators. Moreover, the alternative approach is computationally more expensive with respect to the Pearson correlation coefficients and p-value calculations, as the causality condition in equation 5.17 has to be tested against all the triggered hits in the cluster, this number ranging up to several tens of thousands.

5.2.2 Trigger system

The trigger system implemented within ANTS runs on a single trigger unit. This choice has been done to ease the handling of the trigger results. Conversely, a concurrent trigger system would imply the use of synchronisation and mutual exclusion directives that, if not correctly handled, may drive to errors or halting conditions. On the other hand, the trigger algorithms are, in general, much cheaper, in terms of computing resources, than the reconstruction algorithm, thus a serial processing is affordable and favourable².

Each reconstructed track coming out from the RUs is passed to the TU that executes the pre-defined trigger algorithms, one at a time, against the track.

For what concern trigger algorithms, they must be agreed together with the other experiments, according to the follow-up capability of each observatory, and a Memorandum of Understanding (MoU) must be signed.

Anyhow, the following trigger algorithms have been developed and integrated into the ANTS, for demonstrative purposes:

- the *HighLight* algorithm searches for tracks with number of hits in the cluster exceeding a defined threshold, above a quality threshold; the number of hits is related to the track length, which in turn is related to the energy of the particle;
- the *HotSpot* algorithm searches for a certain number of tracks, all exceeding a quality threshold, within a predefined angular amplitude in a time window of fixed size around the candidate track.

Lastly, a procedure for debug purposes has been added in the queue together with the trigger algorithms, called *Scaler*: it dumps reconstructed tracks one in a tunable number.

²In Donald Knuth's paper "Structured Programming with go to Statements", he wrote: "Programmers waste enormous amounts of time thinking about, or worrying about, the speed of noncritical parts of their programs, and these attempts at efficiency actually have a strong negative impact when debugging and maintenance are considered. We should forget about small efficiencies, say about 97% of the time: **premature optimization is the root of all evil**. Yet we should not pass up our opportunities in that critical 3%."

Chapter 6

Characterisation of ANTS

In this chapter the performances of ANTS are described. The parameters characterising the system are:

- the reconstruction *purity*, i.e. the ability of the reconstruction algorithm to reject the background;
- the reconstruction *efficiency*, that is a number that describes the ability to reconstruct a track;
- the *angular resolution* of the reconstruction algorithm, i.e. the difference between the reconstructed and the real directions;
- the *computation time* required to process an event and provide a result to be sent as an alert.

Studies have been performed with Monte Carlo methods, that are described in section 6.1. Section 6.2 is then dedicated to the study of each of these parameters.

6.1 Monte Carlo

Monte Carlo (MC) simulations are a powerful statistical tool widely used in physics to estimate physical parameters that cannot be evaluated otherwise, either because an exact mathematical model for the problem is not available or because it is impossible to solve it analytically.

The *Monte Carlo truth* is defined as the full set of parameters that characterise the process being studied. The power of the reconstruction system implemented within ANTS is evaluated using the energy and direction of neutrinos and muons as well as the detector response – in terms of the detected hits.

A software chain has been developed to simulate events in the KM3NeT detector [67]. It is subdivided into four main steps:

1. event generation: the relevant processes are simulated in the proximity of the detector, in a wide angular and energy range, and the physics characteristics of the potentially interesting particles – neutrinos or atmospheric muon bundles – are stored.
2. particle and light propagation: particles are propagated through the detector and the light coming from the Čerenkov effect is simulated and propagated to the PMTs;
3. data acquisition simulation: the PMT behaviour, and the data read-out electronics are simulated;
4. data filtering is applied, after having added a combinatorial optical background simulating the effect of ^{40}K decay, as described in subsection 3.3.1. The output at this step is in the same format used for storing real data.

The event generation is performed with the `CORSIKA` [91] or `MUPAGE` [92] codes for atmospheric muons and with the `GENHEN` [93, 94] code for neutrinos. The `KM3` [95] program is used to simulate both the effect of particles propagation in water and the probability of revealing light. `JTriggerEfficiency` is the program that allows simulating the effect of the PMT response, trigger and the processing of raw hits into triggered events.

The simulation method foresees the definition a cylindrical volume, called the *can*, around the detector instrumented volume. It defines the active volume where Čerenkov light can be detected, typically set to three times the light absorption length in water. Particles produced outside the can and not reaching its surface are not further considered in event processing.

The `GENHEN` package, initially created for the `ANTARES` telescope and further developed in `KM3NeT`, is suitable for the full range of neutrino studies from neutrino oscillations to high-energy astrophysics, being the majority of detected neutrinos in a range of energies from tens of GeV, limited by the energy threshold of muon detection of around 10 GeV, to multi-PeV, where the absorption of neutrinos in the Earth, which strongly attenuates the upward neutrino flux, must be taken into account. The *scaled volume*, surrounding the can, is defined as the space that contains all potentially observable neutrino interactions. `GENHEN` generates neutrinos with tunable angular and energy distributions in the scaled volume. If the generated point is outside the can, the shortest distance from the neutrino vertex position to the can is calculated. If this distance is greater than the maximum muon range for that neutrino energy, the event is rejected and not further processed.

`CORSIKA` is a program for the simulation of primary cosmic rays in the atmosphere. In `KM3NeT` it is used to provide accurate informations about muons and neutrinos produced in extensive air showers, which represent a source of background. The minimum altitude that can be treated by

`CORSIKA` is the sea level. Propagation simulation of muons up to the can level is provided by the `MUSIC` program [96], while neutrino trajectories are projected geometrically. `MUPAGE` [92] is alternatively used to generate muons directly at the can level. It uses parametrisations obtained with the data from the `MACRO` [97, 98] experiment to calculate the muon flux at the desired depth in water or ice.

For what concerns the handling of physical phenomena within the can, the `KM3` program simulates the particle interaction and their light emission, while for muons energy loss `MUSIC` is used. It divides the path of each particle into steps of fixed length. At each step, the energy and position of the particle is updated taking into account all possible interactions with the medium and a profile of the number of photons reaching various distances from the path segment is provided. The angular acceptance of such photons on the PMTs is also evaluated.

Eventually, `JTriggerEfficiency` is the program devoted to the simulation of photon hit detection, digital conversion and trigger. It also adds a combinatorial background, simulating the effect of ^{40}K decay. Its output is in the same `ROOT` format used by the on-line trigger system. This feature allows transparent processing of either real and MC data with the same codes.

6.2 Reconstruction

A dedicated program, called `RECANT`, including all functionalities of a standard reconstruction unit has been developed. It allows disentanglement between the RU procedures and the rest of the system in order to perform a simpler and more controlled benchmark. Indeed, it is a serial program: it allows processing of only one event at a time. Triggered events are read from post trigger files produced by the `JTriggerEfficiency` program at the end of the standard Monte Carlo chain. The output of `RECANT` is a table containing detailed information about several internal steps as well as the normal `ANTS`'s output. These additional information include the time, with μs resolution, spent for processing a triggered event, the number of hits per cluster, and the list of centroids.

Another program integrates the `RECANT` output table with the Monte Carlo truth, i.e. the energy of neutrinos and muons and the real direction. This program has been developed separately in order to avoid “interference” between the MC truth and the simulated detector data by design.

The studies presented in the following sections have been performed running `RECANT` against a wide set of MC files, that have been taken from the official `KM3NeT` Monte Carlo production for a half cubic kilometre detector (the building block, see figure 6.1) presented in the Letter of Intent (LoI) of `KM3NeT 2.0` [67]. The production generally comprises two subsets of files:

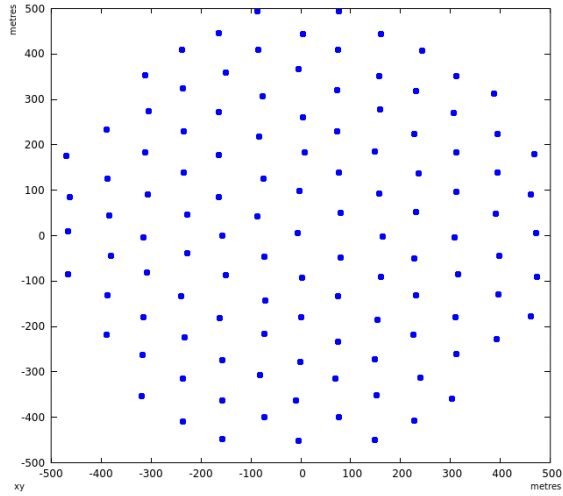


Figure 6.1: Footprint of the detector used in Monte Carlo production. The detector is made of 115 strings (the blue dots) within a cylinder-shaped volume of about 500 metres radius and 700 metres high, i.e. a building block.

- muon neutrino charged current events with 4π uniform angular distribution and power-law energy spectrum $E^{-1.4}$;
- atmospheric muon events with angular and energy distributions provided by MUPAGE.

The muon neutrino data set contains 400 files, 200 with neutrino and an equal number of antineutrinos, each of them providing about 2300 triggered events, in a wide energy range from 10^2 to 10^8 GeV.

On the other side, 1800 atmospheric muon files each containing about 8000 triggered events. The atmospheric muon angular and energy distributions are extrapolated using the MUPAGE program to match those for a detector located 3500 metres below the sea level. The *lifetime*¹ of the sample corresponds to three years above 50 TeV and four months above 1 TeV

In the following sections the results of the characterisation studies are reported. Where applicable and appropriate, the results are shown considering also quality cuts. The *Standard Quality Cut* (SQC) is defined as:

$$q \geq 0.95 \cup p \leq 0.1 \tag{6.1}$$

where p and q are defined in equation 5.14 and equation 5.13. The SQC is the optimal condition for a good resolution with minimal loss of efficiency.

¹The lifetime is the time that a detector would require to be exposed to the same amount of events.

6.2.1 Purity

To study the purity of the reconstruction algorithm, two facts must be considered:

1. the on-line trigger has itself a non-perfect purity. This means that events made of background hits only may occur. The ANTS' minimum requirements allow to reject these spurious events;
2. the output of the reconstruction of atmospheric muon events (downward-going) has not to mime the neutrino signal (upward-going).

Generally, the purity of a selection algorithm operating on a sample of events is:

$$P = \frac{N_{sig}^{sel}}{N^{sel}} \quad (6.2)$$

where N_{sig}^{sel} is the number of selected signal events and N^{sel} is the number of total selected events, both signal and background. From a frequentist perspective, the purity P represents the probability to correctly identify a signal event. Its opposite, $P^{wrong} = 1 - P$, represents the probability to misidentify a background event as signal.

In case of ANTS, the global “mismatch” probability is defined as:

$$P^{wrong} = P_{trig}^{wrong} + \left(1 - P_{trig}^{wrong}\right) \cdot P_{rec}^{wrong} \quad (6.3)$$

where P_{trig}^{wrong} is the probability of reconstructing a triggered event completely made of background hits and P_{rec}^{wrong} is the probability of reconstructing a downward-going atmospheric muon as upward-going. The global purity is thus given by:

$$P = 1 - P^{wrong} \quad (6.4)$$

In order to estimate P_{trig}^{wrong} a dedicated Monte Carlo has been produced and the results are shown in table 6.1. For a given detector, the `JRandomTimesliceWriter` program provides simulated timeslices (100 ms each). The time of the hits on each PMT is distributed according to a Poisson distribution with user defined rate. The `JTriggerProcessor` program, another clone of the on-line trigger program, is fed with the output of `JRandomTimesliceWriter` and produces a standard ROOT file.

None of the triggered events passed the reconstruction cuts implemented by ANTS. A naïve interpretation of this result is that the system provides a perfect purity. Despite the fact that this is probably not too far from the truth, since the probability of a pure background event has to “mime” that of a muon is very low, the simulated sample is limited to ten thousands timeslices due to computation problems. The size of this production already exceeds several hundreds gigabytes and required weeks of CPU time. For

Hit rate	Triggered events	Reconstructed events
5.0 kHz	30	0
7.5 kHz	139	0
10.0 kHz	718	0
12.5 kHz	2976	0
15.0 kHz	11000	0
17.5 kHz	35868	0
20.0 kHz	106820	0

Table 6.1: Official trigger and ANTS reconstruction run on simulation of pure ^{40}K background for various hit rates. For each run 10^4 timeslices have been simulated. No one of the triggered events passed the reconstruction requirements.

those reasons, a more detailed study may lead to a different and more accurate result, but this is beyond the aim of this work.

For what concerns the second step of purity estimation, $(1 - P_{rec}^{wrong})$, the atmospheric muon MC production has been used. In figure 6.2 the fraction of reconstructed tracks with zenith angle less than 90° is reported as a function of the muon energy for no quality cuts and applying the Standard Quality Cut.

Also in this case the results lead to a very high level purity, that is always greater than 95% for all reconstructed muons and almost 100% in the case of those passing the quality filter. In figure 6.3 the reconstruction purity as a function of the cosine of the Monte Carlo zenith angle is shown. Values of -1 and 0 correspond to perfectly vertical and horizontal direction, respectively. The graph shows that the maximum purity is for horizontal muons. This is due to the fact that horizontal muons are highly energetic, thus better reconstructed than the vertical counterpart, that, on the other hand, allows also a less energetic component. Also, the KM3NeT DOM exposes less PMTs upwards than in the downward direction, thus resulting in a smaller sensitivity to downward-going particles. Moreover, the number of DOMs that a vertical muon encounters along its path is larger than that of a horizontal muon, in the case of equal energy at the detector boundary, the vertical distance between adjacent DOMs being smaller than the horizontal one.

Unfortunately, no code for the simulation of bioluminescence phenomena is currently available. The purity with respect to this kind of background, sporadic but indeed compelling, can be studied only with real data.

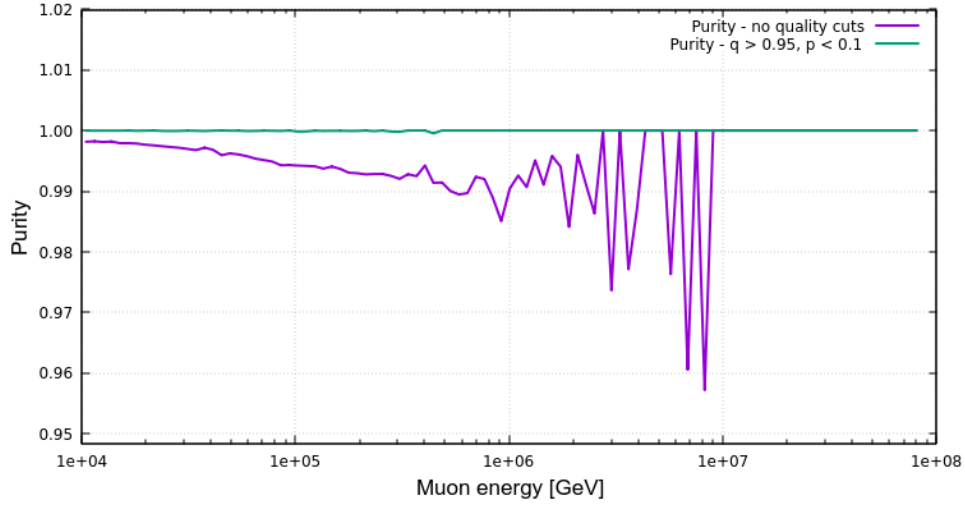


Figure 6.2: Reconstruction purity ($1 - P_{rec}^{wrong}$) as a function of the energy of the muon. Magenta and green lines represent the global purity and that applying $q \geq 0.95 \cup p \leq 0.1$ quality cuts, respectively.

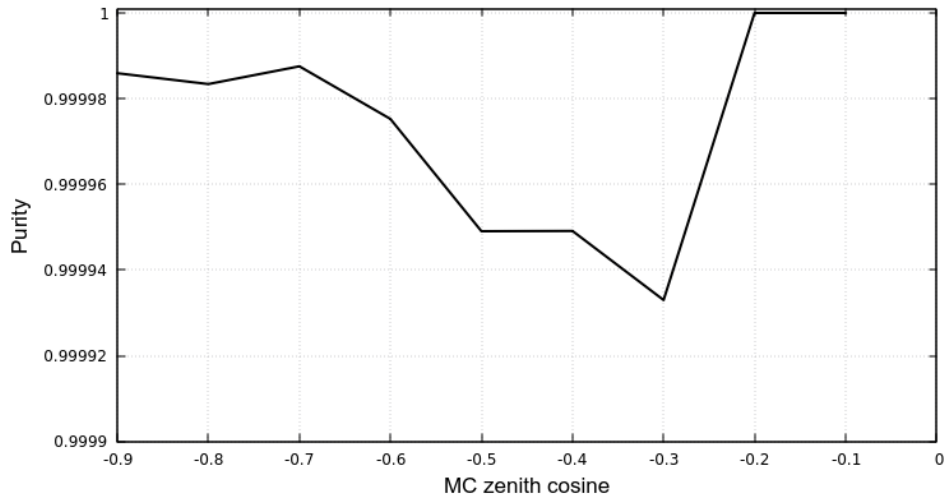


Figure 6.3: Reconstruction purity ($1 - P_{rec}^{wrong}$) as a function of the cosine of MC zenith angle of the muon. Data filtered purity with $q \geq 0.95 \cup p \leq 0.1$ quality cuts.

6.2.2 Efficiency

The efficiency ε of a filtering procedure acting on a set of events (signal+background) is defined by:

$$\varepsilon = \frac{N_{sig}^{sel}}{N_{sig}} \quad (6.5)$$

where N_{sig}^{sel} is the number of selected signal events and N_{sig} is the number of signal events. The neutrino MC sample has been used to make an estimation of the efficiency of the reconstruction algorithm as a function of the energy of the neutrino.

In figure 6.4 the reconstruction efficiency for high energy (≥ 100 TeV) neutrinos is shown as a function of the two quality parameters. As expected, it decreases as q increases and as p decreases.

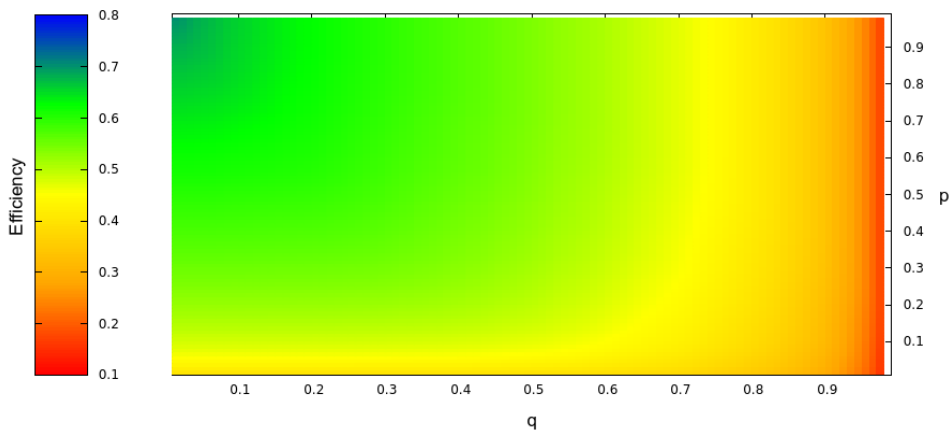


Figure 6.4: Heat map of the reconstruction efficiency for neutrinos with energy ≥ 100 TeV as a function of the two quality parameters.

Figure 6.5 shows the efficiency curves both in the case of bare reconstruction, i.e. without any quality cut, and in the case of the SQC, $q \geq 0.95 \cup p \leq 0.1$. In the latter case, the selection criterion is the union of the ANTS' minimum requirements plus the quality cuts, i.e. N_{sig}^{sel} is the number of events either effectively reconstructed and passing the quality cuts.

A drop in the efficiency is visible at high energy in the curve where cuts are applied. This is an issue due to the following fact: a high-energy muon is able to go through the whole detector volume and edge effects start to take place such that the centroids calculated nearby the borders of the detector don't match with a straight line any more. In figure 6.6 four plots are shown: triggered hits are represented by blue asterisks and the centroids passing the minimum requirements are shown in red circles. Most of the hits belong to the same cluster. The third plot, bottom-left, shows the projection of

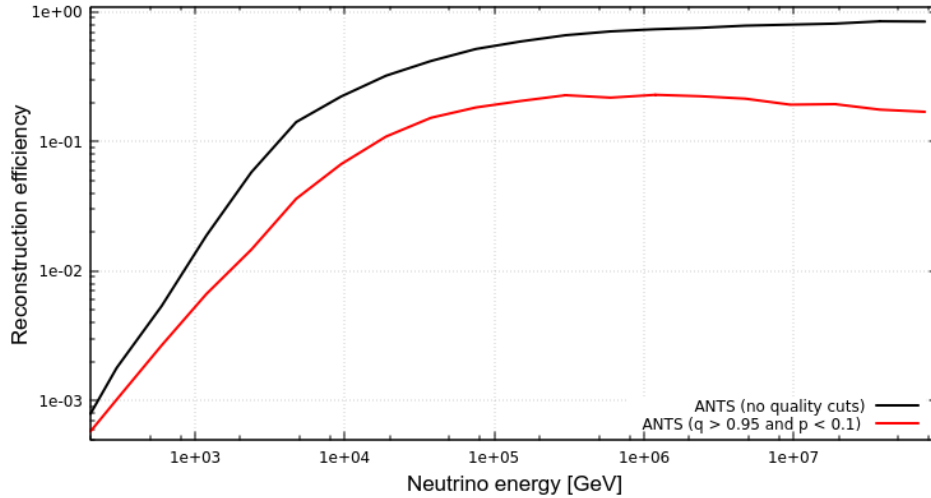


Figure 6.5: ANTS reconstruction efficiency as a function of the neutrino energy with no quality cuts (black line) and with $q \geq 0.95 \cup p \leq 0.1$ quality cuts (red line).

the event in the zt plane. The particle, an up-going muon from 60 PeV ν_μ CC interaction, crosses the top surface of the detector, at $z = 700$ m. As a result, 6 out of 16 centroids are out of the main trend. The resulting quality parameters are $q = 0.38$ and $p = 0.06$, thus does not pass the quality cuts.

This issue might be cured by introducing an alternative quality parameter, like the one suggested in section 5.2.1. Another possibility is to define a *fiducial detector volume*. In the latter situation, the detector volume is round by its extremes. Centroids placed outside the fiducial volume are removed. Care must be taken during this operation as perfectly vertical events outside the fiducial volume would be discarded even if a good reconstruction can be performed. This would make the code more complicated and difficult to test as a dedicated MC would be required.

In order to compare ANTS with the official KM3NeT reconstruction software, called `recoLNS`, figure 6.7 shows the efficiency of both systems. `recoLNS` implements a very complex algorithm, with four subsequent fit steps, providing an angular resolution of about 0.1° [67]. Detailed information can be found in [69].

The ANTS' curves in figure 6.7 generally show a higher efficiency in a wide neutrino energy range with respect to that of `recoLNS` with higher purity (yellow solid line).

6.2.3 Angular resolution

As an estimate of the angular resolution, the median of the total angle between the muon direction from MC truth and that provided by the recon-

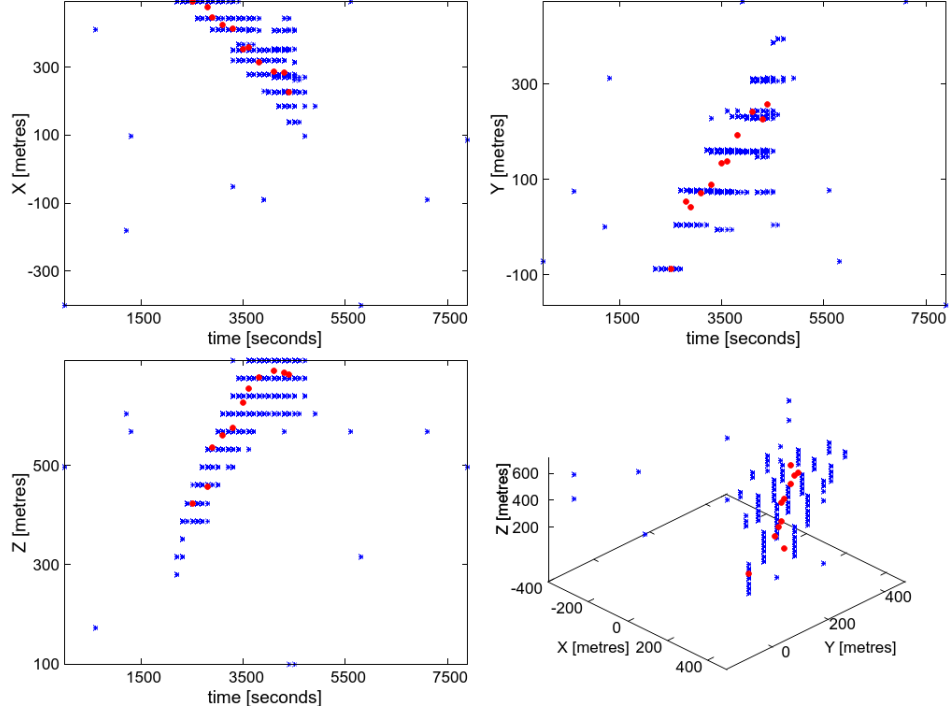


Figure 6.6: Pathological ν_μ CC event. Top-left, top-right, and bottom-left show the projections of the triggered hits (blue asterisks) and the selected centroids (red circles) in the xt , yt , and zt planes, respectively. The bottom-right plot shows the event in a 3D space.

struction is used. This angle, $\Delta\vartheta$, is calculated as:

$$\Delta\vartheta = \arccos\left(\frac{\vec{v} \cdot \vec{v}_{\text{truth}}}{|\vec{v}| |\vec{v}_{\text{truth}}|}\right) \quad (6.6)$$

where \vec{v}_{truth} is the MC true direction and \vec{v} is the reconstructed one.

Figure 6.8 shows $\Delta\vartheta$ as a function of the neutrino energy. The gold and light green bands represent the 90% and 68% quantiles of the $\Delta\vartheta$ distribution, respectively. The median value is about 2° for the whole energy range. As already stated in the previous section, the official KM3NeT reconstruction software presents a much better angular resolution, but at the cost of a computation time of the order of minute per event.

In figure 6.9 an heat map of the angular resolution is shown as a function of the quality parameters used in cuts. Also in this case, the SQC determines an optimal condition. In the worst condition, i.e. with no quality cuts, the angular resolution is about 4° .

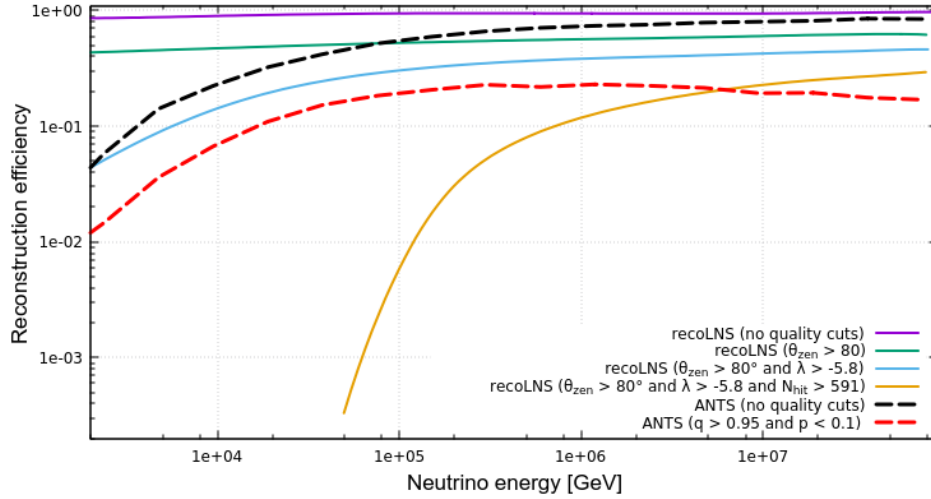


Figure 6.7: Reconstruction efficiency of ANTS with no quality cuts (black dashed line) and with $q \geq 0.95 \cup p \leq 0.1$ quality cuts (red dashed line), of recoLNS with no quality cuts (purple solid line), with $\theta_{\text{zen}} > 80^\circ$ (green solid line), with $\theta_{\text{zen}} > 80^\circ \cup \lambda > -5.8$ (cyan solid line), and with $\theta_{\text{zen}} > 80^\circ \cup \lambda > -5.8 \cup N_{\text{hits}} > 591$, as a function of the neutrino energy.

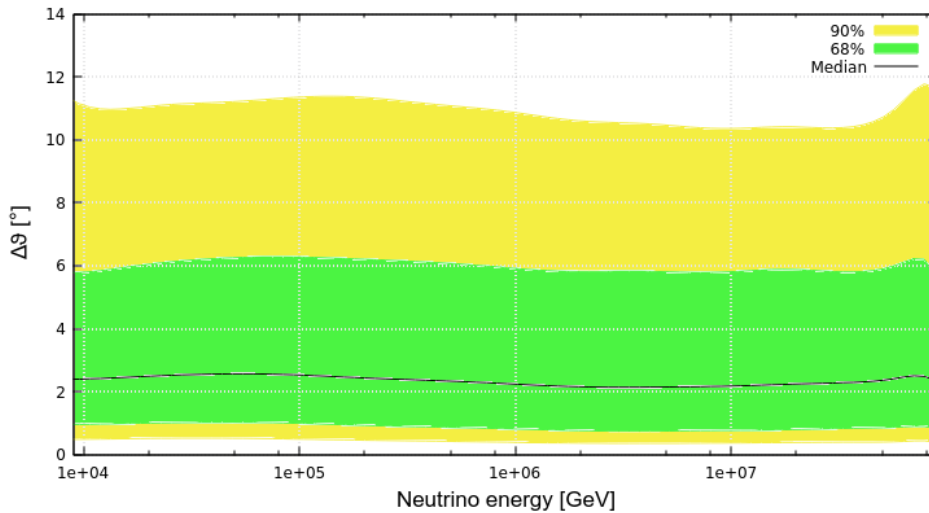


Figure 6.8: Median (black solid), 68% (green band) and 90% (yellow band) percentiles of $\Delta\vartheta$ as a function of the neutrino energy. The SQC is applied. See the text.

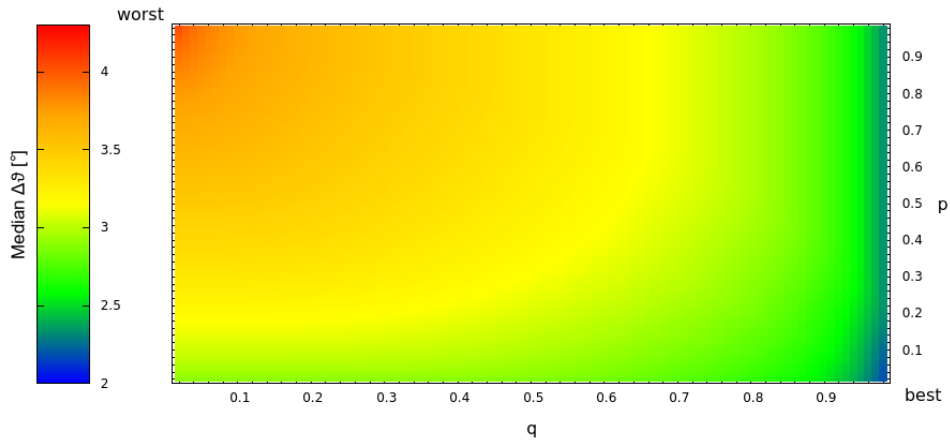


Figure 6.9: Heat map of the angular resolution (median of $\Delta\vartheta$) as a function of the applied quality cuts.

6.2.4 Performances

The possibility to perform multi-messenger studies is fundamentally linked to the ability to deliver alerts as soon as possible. CPU usage, i.e. the time spent by the program to be run, is a cardinal point for the success of the mission the ANTS project aims to. The time required by the reconstruction algorithm has been measured for each MC triggered event in a qualified and monitored environment. Indeed, the *HEP-SPEC06* [99] score has been provided. HEP-SPEC06 is the HEP²-wide benchmark for measuring CPU performance. Its goal is to provide a consistent and reproducible CPU benchmark to describe experiment requirements, laboratory commitments, existing compute resources, as well as procurements of new hardware. Although the HEP-SPEC06 benchmark was initially designed to meet the requirements of high-energy physics laboratories, it is widely used also by other communities. HEP-SPEC06 is based on the *all_cpp* benchmark subset (*bset*) of the industry standard SPEC[®] [100] CPU2006 benchmark suite, that matches the percentage of floating point operations which have been observed in batch jobs ($\sim 10\%$), and it scales perfectly with the experiment codes.

The system adopted for benchmark is a dedicated server machine hosting two 64-bits Intel[®] Xeon[®] E5520 CPUs with 4 cores each and Hyper-Threading³ enabled, clock frequency of 2.27 GHz and 12 GB of DDR3 RAM memory operating at 1333 MHz. The operating system is *Scientific Linux*, version 6.4 (Carbon), a GNU/Linux distribution designed to ship scientific tools and programming libraries as well as to provide high stability and

²High Energy Physics

³Intel's[®] Hyper-Threading Technology (HTT) provides two threads of execution for each physical core. Applications can run faster doing more operation in parallel exploiting many threads.

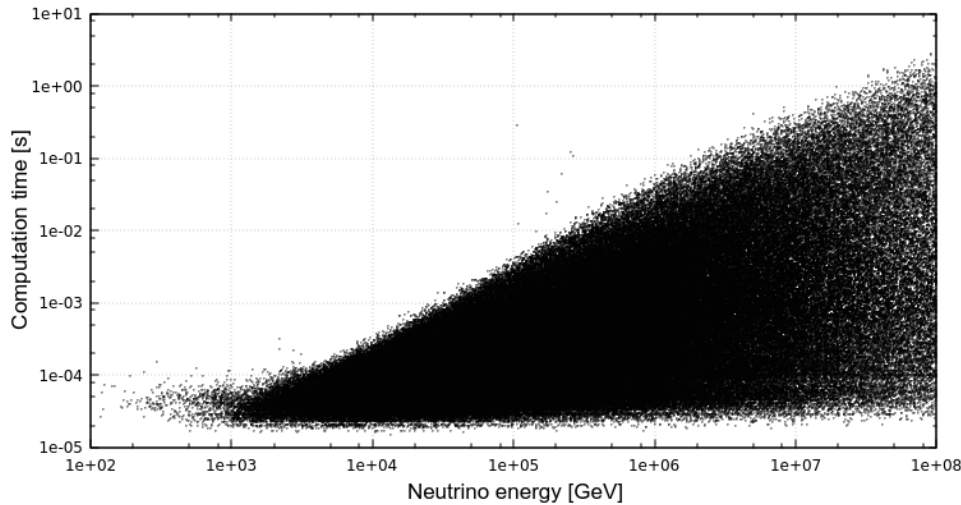


Figure 6.10: Scatter plot of the CPU time to process single events versus the energy of the simulated neutrino.

quality. For such system the HEP-SPEC06 score is $127 \div 128$ [101].

Figure 6.10 shows the scatter plot of the time spent by the reconstruction unit to process a triggered event versus the energy of the neutrino. It is a wide area ranging from 10^2 to 10^8 GeV in energy and from less than $1 \mu\text{s}$ to about 2 seconds in time. The area has an upper limit given by a straight-line, that defines the worst computation time for a given neutrino energy, linearly dependent to the neutrino energy itself. The spread under this worst case is given by two facts:

- the computation time is – roughly – proportional to the number of triggered hits forming the event, this number depending on the geometrical relationship between the track and the detector, such as the track length, the direction and the entry point into the detector volume;
- the energy transfer from the neutrino to the muon is a stochastic process, as described in subsection 2.1.1;

In figure 6.11 the event processing time versus the number of hits is shown. The shape is almost linear, with some spread probably due to the presence of background hits. Even though the contribution of these hits to the total number of hits is almost negligible, they contributes in terms of almost-empty hit clusters, to an extent comparable to the number of background hits itself. Each cluster has to be processed and, even if it is immediately removed, some time must be spent on each of them. The spread decreases as the number of hits increases. The more the number of hits due to the signal, the more the probability to include background hits in the leading cluster.

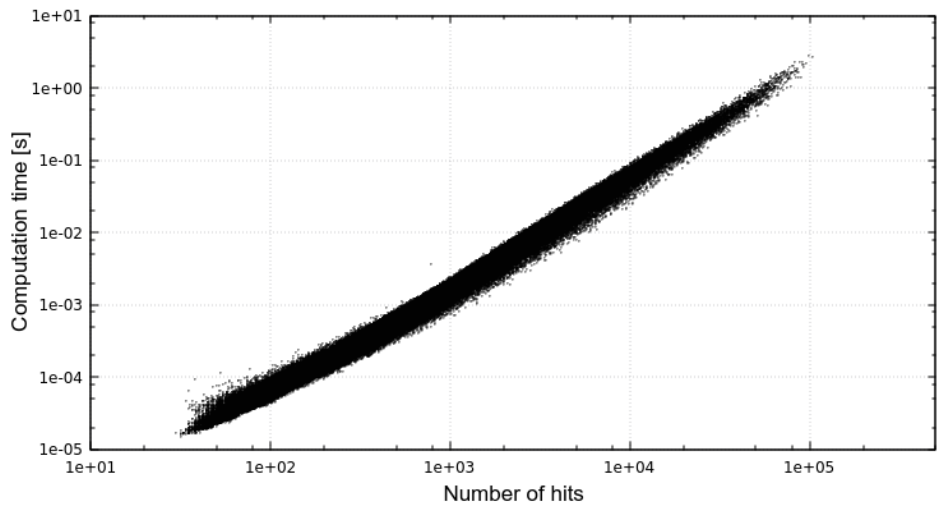


Figure 6.11: Scatter plot of the CPU time to process single events versus the total number of hits in the event.

Conclusions

Neutrino astronomy is a very promising research field within the particle astrophysics. It represents a powerful tool for shedding light on the most energetic events in the Universe.

In 2013, the IceCube telescope already proved the existence of a flux of extreme high-energy neutrinos of cosmic origin, but the poor angular resolution of the detector did not allow to find an astrophysical neutrino source yet. Moreover, its position in the southern hemisphere limits its capability to detect events from interesting regions, e.g. the Galactic Centre.

The KM3NeT project aims to build a network of new generation neutrino detectors in the Mediterranean Sea. The ORCA, being constructed off Toulon in France, is devoted to the study of the neutrino mass hierarchy exploiting the oscillation of atmospheric neutrinos. The ARCA neutrino telescope aims at the study of high-energy cosmic neutrinos exploiting the Čerenkov light from the neutrino interaction products. It provides the great opportunity to perform measurements of the flux of such extreme energy neutrinos with unprecedented angular resolution, to search for their sources, providing invaluable information about the mechanisms acting in their inner cores. The ARCA detector, whose construction started in December 2015, off Portopalo di Capo Passero, Sicily, will be constituted by several hundreds thousands of light sensors, i.e. photomultiplier tubes, hosted in hundreds of vertical structures, called Detection Units. The Digital Optical Module, DOM, hosting 31 PMTs looking at all directions, is at the basis of the technological improvement made by KM3NeT with respect to its predecessors. The ARCA detector data are dominated by the background mainly due to potassium-40 (^{40}K) and atmospheric muons and neutrinos as well as occasional bioluminescence phenomena. The use of an on-line trigger system, called TriDAS, is required in order to select interesting events from the enormous data flux, improving the signal to noise ratio. Beyond this, with KM3NeT ARCA, will be possible to perform multi-messenger analyses via follow-up observations by other experiments, via photons (optical, X , γ), cosmic rays, and gravitational waves.

Multi-messenger studies, driven by follow-up observations, allow to detect transient phenomena from the rapidly fading sources like gamma ray bursts, reducing the systematic errors.

The ANTS system, presented and discussed in this thesis, has been implemented to allow fast neutrino alerting by means of a new track reconstruction method. It is based on the events coming out from the on-line trigger system. A clustering algorithm, based on simple space-time causality criteria, allows grouping PMT hits that are likely to be caused by Čerenkov photons emitted along the path of a highly energetic muon in water. A temporal partition, made of equal-duration temporally disjoint subsets of hits, is built upon the cluster and for each partition element a centroid, the centre of mass and average time of the hits, is calculated. The track direction is reconstructed by means of a linear fit procedure over the centroids. Selections are performed on the set of centroids in order to remove the outliers. An estimator has been developed to represent the quality of the cluster. It provides a powerful tool to awfully improve the purity of the final track sample.

The ANTS' computation performances allow sending alert messages with few seconds delay, according to the specifications of the machine used in the tests, with respect to the physical event, at the cost of very few computation units also when dealing with a cubic kilometre-sized detector. Moreover, the angular resolution of some degree together with an high purity make it suited for multi-messenger studies.

Improvements to the ANTS system can be generally achieved. Higher efficiency of both high-energy and low-energy neutrino reconstruction can be obtained by introducing a more refined hit clustering algorithm. Also, an optimisation of the quality cuts, based on the number of input hits, can be done. In case of events with a large number of hits, the quality thresholds can be relaxed resulting in a higher efficiency. Moreover, by means of stronger centroids filtering criteria, both the reconstruction efficiency and the angular resolution can be enhanced. The event processing time, even though already better than that of competitor algorithms, would be improved by utilising more recent hardware, operating system and C++ compiler. Indeed, recent revisions of the C++ programming language allow the compilers to better optimise the final machine code. Anyway, a speed-up of at least 40% is expected when running the software on the current shore-station computing infrastructure.

Finally, it is possible to extend the set of observables carried by the alert message with other important information, such as the estimation of the muon energy and of the path length together with the determination of the interaction point, taking profit of already existing programs.

Bibliography

- [1] V. F. Hess. Über Beobachtungen der durchdringenden Strahlung bei sieben Freiballonfahrten. *Physik. Zeitsc.*, 13:1084–1091, 1912.
- [2] C. D. Anderson. The positive electron. *Phys. Rev.*, 43:491–494, 1933.
- [3] S. H. Neddermeyer and C. D. Anderson. Note on the nature of cosmic-ray particles. *Phys. Rev.*, 51:884–886, 1937.
- [4] C. M. G. Lattes, H. Muirhead, G. P. S. Occhialini, and C. F. Powell. Processes involving charged mesons. *Nature*, 159:694–697, 1947.
- [5] J. Blümer, R. Engel, and J. R. Hörandel. Cosmic rays from the knee to the highest energies. *Progress in Particle and Nuclear Physics*, 63:293–338, 2009.
- [6] M. Longair. *High Energy Astrophysics*. Cambridge University Press, Cambridge, 1992.
- [7] A. M. Hillas. Cosmic rays: Recent progress and some current questions. 2006.
- [8] J. R. Hörandel. The composition of cosmic rays at the knee. *AIP Conference Proceedings*, 1516(1):185–194, 2013.
- [9] R. Aloisio, V. Berezhinsky, and A. Gazizov. Transition from galactic to extragalactic cosmic rays. *Astrop. Phys.*, 39-40:129 – 143, 2012. Cosmic Rays Topical Issue.
- [10] K. Greisen. End to the cosmic-ray spectrum? *Phys. Rev. Lett.*, 16:748–750, 1966.
- [11] G. T. Zatsepin and V. A. Kuz'min. Upper Limit of the Spectrum of Cosmic Rays. *JTEP*, 4:78, 1966.
- [12] M. Spurio. *Particles and Astrophysics*. Springer, Berlin, 2014.
- [13] E. Fermi. On the origin of the cosmic radiation. *Phys. Rev.*, 75:1169, 1949.

- [14] A. R. Bell. The acceleration of cosmic rays in shock fronts. I. *MNRAS*, 182:147–156, 1978.
- [15] P. Lipari. Introduction to neutrino physics, 2003. <http://cds.cern.ch/record/677618>.
- [16] P. Meszaros. Gamma-Ray Bursts. *Rept. Prog. Phys.*, 69:2259–2322, 2006.
- [17] C. K. Seyfert. Nuclear Emission in Spiral Nebulae. *Astrophysical Journal*, 97:28, 1943.
- [18] Close-up Look at a Jet near a Black Hole in Galaxy M87. <https://www.spacetelescope.org/images/opo9943b/>.
- [19] R. Antonucci. Unified models for active galactic nuclei and quasars. *Annu. Rev. of Astron. Astrophys.*, 31:473–521, 1993.
- [20] C. M. Urry and P. Padovani. Unified Schemes for Radio-Loud Active Galactic Nuclei. *ASP*, 107:803, 1995.
- [21] The Pierre Auger Collaboration. Update on the correlation of the highest energy cosmic rays with nearby extragalactic matter. *Astrop. Phys.*, 34(5):314 – 326, 2010.
- [22] J. Abraham et al. Observation of the suppression of the flux of cosmic rays above $4 \cdot 10^{19}$ eV. *Phys. Rev. Lett.*, 101:061101, 2008.
- [23] M. Takeda et al. Extension of the Cosmic-Ray Energy Spectrum beyond the Predicted Greisen-Zatsepin-Kuz'min Cutoff. *Phys. Rev. Lett.*, 81:1163–1166, 1998.
- [24] R. U. Abbasi et al. First observation of the greisen-zatsepin-kuzmin suppression. *Phys. Rev. Lett.*, 100:101101, 2008.
- [25] A. I. Nikishov. Absorption of high-energy photons in the universe. *JTEP*, 14:393, 1962.
- [26] R. Gandhi, C. Quigg, M. H. Reno, and I. Sarcevic. Ultrahigh-energy neutrino interactions. *Astrop. Phys.*, 5(2):81 – 110, 1996.
- [27] R. Gandhi, C. Quigg, M. H. Reno, and I. Sarcevic. Neutrino interactions at ultrahigh energies. *Phys. Rev. D*, 58:093009, 1998.
- [28] V. S. Berezhinsky and A. Z. Gazizov. *JTEP*, 33:120, 1981.
- [29] S. L. Glashow. Resonant scattering of antineutrinos. *Phys. Rev.*, 118:316–317, 1960.

- [30] J. D. Jackson. *Classical Electrodynamics (3rd ed)*. John Wiley & Sons, 1998.
- [31] J. G. Learned and K. Mannheim. High-energy neutrino astrophysics. *Ann. rev. nucl. part. sci.*, pages 679–749, 2000.
- [32] G. Riccobene et al. Deep seawater inherent optical properties in the southern ionian sea. *Astrop. Phys.*, 27(1):1 – 9, 2007.
- [33] IceCube Collaboration. Icecube web site. <https://icecube.wisc.edu>.
- [34] Antares Collaboration. Antares web site. <http://antares.in2p3.fr>.
- [35] Baikal Collaboration. Baikal web site. <http://www.inr.ru/eng/ebgnt.html>.
- [36] G. A. Askaryan. Excess negative charge of an electron-photon shower and its coherent radio emission. *Soviet Journal of Experimental and Theoretical Physics*, 41:616, 1961.
- [37] D. Saltzberg. Observation of the Askaryan effect: Coherent microwave Cherenkov emission from charge asymmetry in high-energy particle cascades. *Phys. Rev. Lett.*, 86:2802–2805, 2001.
- [38] P. W. Gorham and other. Accelerator measurements of the Askaryan effect in rock salt: A Roadmap toward teraton underground neutrino detectors. *Phys. Rev.*, D72:023002, 2005.
- [39] P. W. Gorham et al. Observations of the Askaryan effect in ice. *Phys. Rev. Lett.*, 99:171101, 2007.
- [40] G. A. Askaryan. Coherent Radio Emission from Cosmic Showers in Air and in Dense Media. *Soviet Journal of Experimental and Theoretical Physics*, 21:658, 1965.
- [41] G. M. Frichter and other. On radio detection of ultrahigh energy neutrinos in antarctic ice. *Phys. Rev. D*, 53:1684–1698, 1996.
- [42] P. Allison et al. IceRay: An IceCube-centered radio-Cherenkov GZK neutrino detector. *Nucl. Instrum. Meth. A*, 604:S64 – S69, 2009. ARENA 2008.
- [43] G.A. Askaryan. Hydrodynamic radiation from the tracks of ionizing particles in stable liquids. *The Soviet Journal of Atomic Energy*, 3:921–923, 1957.
- [44] C. Pellegrino. Rivelazione di segnali acustici con telescopi sottomarini per neutrini astrofisici di altissima energia. Implementazione dei sistemi di rivelazione e acquisizione per i progetti KM3NeT e SMO/NEMO-Phase II. Master’s thesis, Università degli studi di Catania, 2013.

- [45] J.A. Aguilar et al. AMADEUS - The acoustic neutrino detection test system of the ANTARES deep-sea neutrino telescope. *Nucl. Instrum. Meth. A*, 626-627:128 – 143, 2011.
- [46] T. Chiarusi and M. Spurio. High-energy astrophysics with neutrino telescopes. *EPJ C*, 65:649–701, 2010.
- [47] Thomas K. Gaisser, Francis Halzen, and Todor Stanev. Particle astrophysics with high energy neutrinos. *Phys. Rep.*, 258(3):173 – 236, 1995.
- [48] K. A. Olive et al. Review of Particle Physics. *Chin. Phys.*, C38:090001, 2014.
- [49] M.A. Markov and I.M. Zheleznykh. On high energy neutrino physics in cosmic rays. *Nucl. Phys.*, 27(3):385 – 394, 1961.
- [50] Dumand web site. <http://www.phys.hawaii.edu/dumand/>.
- [51] I.A Belolaptikov and et. al. The baikal underwater neutrino telescope: Design, performance, and first results. *Astrop. Phys.*, 7(3):263 – 282, 1997.
- [52] V. Aynutdinov and the Baikal Collaboration. Search for a diffuse flux of high-energy extraterrestrial neutrinos with the NT200 neutrino telescope. *Astropart. Phys.*, 25:140–150, 2006.
- [53] A. V. Avrorin and the Baikal Collaboration. An experimental string of the NT1000 Baikal neutrino telescope. *Instr. Exp. Techn.*, 54(5):649–659, 2011.
- [54] A. Achterberg and The IceCube Collaboration. First year performance of the IceCube neutrino telescope. *Astrop. Phys.*, 26(3):155 – 173, 2006.
- [55] M. G. Aartsen et al. First Observation of PeV-Energy Neutrinos with IceCube. *Phys. Rev. Lett.*, 111:021103, 2013.
- [56] M. G. Aartsen et al. Evidence for High-Energy Extraterrestrial Neutrinos at the IceCube Detector. *Science*, 342(6161), 2013.
- [57] M. G. Aartsen et al. Neutrinos and Cosmic Rays Observed by IceCube. 2017. ARXIV:1701.03731.
- [58] M. G. Aartsen et al. Flavor Ratio of Astrophysical Neutrinos above 35 TeV in IceCube. *Phys. Rev. Lett.*, 114(17):171102, 2015.
- [59] M. G. Aartsen et al. All-sky search for time-integrated neutrino emission from astrophysical sources with 7 years of IceCube data. 2016. ARXIV:1609.04981.

- [60] NEMO web site. <http://www.nemoweb.lns.infn.it/>.
- [61] SMO web site. <http://web.infn.it/smo>.
- [62] S. Viola, F. Simeone, and M. Saldaña. Characterisation and testing of the KM3NeT acoustic positioning system. *EPJ Web of Conferences*, 116:03006, 2016.
- [63] T. Chiarusi et al. Status and first results of the NEMO Phase-2 tower. *JINST*, 9(03):C03045, 2014.
- [64] S. Aiello et al. Measurement of the atmospheric muon depth intensity relation with the NEMO Phase-2 tower. *Astrop. Phys.*, 66:1 – 7, 2015.
- [65] G. Aggouras et al. A measurement of the cosmic-ray muon flux with a module of the NESTOR neutrino telescope. *Astrop. Phys.*, 23:377–392, 2005.
- [66] KM3NeT Collaboration. Conceptual design report, 2011. <http://www.km3net.org/TDR/KM3NeTprint.pdf>.
- [67] S. Adrian-Martinez et al. Letter of intent for KM3NeT 2.0. *J. Phys.*, G43(8):084001, 2016.
- [68] KM3NeT Collaboration. KM3NeT website. <http://www.km3net.org>.
- [69] A. Trovato. *Development of reconstruction algorithms for large volume neutrino telescopes and their application to the KM3NeT detector*. PhD thesis, Università degli Studi di Catania, Catania, 2013.
- [70] M. Circella, P. Coyle, and P. Kooijman. The Digital Optical Module (DOM) for the KM3NeT Detector. *Proceedings to the 33rd ICRC, Rio de Janeiro*, 2013.
- [71] D. Real. KM3NeT Digital Optical Module electronics. *EPJ Web of Conferences*, 116:05007, 2016.
- [72] S. Adrián-Martínez et al. The prototype detection unit of the KM3NeT detector. *EPJ C*, 76(2):54, 2016.
- [73] KM3NeT Collaboration. Technical description of the PPM of the KM3NeT detection unit, 2010. http://www.km3net.org/PPM/KM3NeT_FL_REP_PPM-description.pdf.
- [74] S. Adrián-Martínez et al. A method to stabilise the performance of negatively fed KM3NeT photomultipliers. *Journal of Instrumentation*, 11(12):P12014, 2016.
- [75] E. Tamburini and other. Deep-sea bioluminescence blooms after dense water formation at the ocean surface. *PLOS ONE*, 8(7):1–10, 2013.

- [76] White rabbit web site. <http://www.ohwr.org/projects/white-rabbit>.
- [77] P. Ferrari, A. Flammini, D. Marioli, and A. Taroni. Ieee 1588-based synchronization system for a displacement sensor network. *IEEE Transactions on Instrumentation and Measurement*, 57(2):254–260, 2008.
- [78] G. E. Moore. Cramming more components onto integrated circuits. *Electronics Magazine*, page 4, 1965.
- [79] ROOT web site. <http://root.cern.ch/>.
- [80] R. Gurin and A. Maslennikov. Controlhost: Package for distributed data handling. *CASPUR Inter-University Computing Consortium Rome*, 1995.
- [81] Bozza, C. The Control Unit of KM3NeT data acquisition. *EPJ Web of Conferences*, 116:05001, 2016.
- [82] Albert, A. and Bozza, C. The relational database system of KM3NeT. *EPJ Web of Conferences*, 116:07004, 2016.
- [83] Gal, T. Live monitoring and quasi-online event reconstruction for KM3NeT. *EPJ Web of Conferences*, 116:05003, 2016.
- [84] J. A. Aguilar et al. A fast algorithm for muon track reconstruction and its application to the ANTARES neutrino telescope. *Astropart. Phys.*, 34:652–662, 2011.
- [85] M. G. Aartsen et al. Observation and Characterization of a Cosmic Muon Neutrino Flux from the Northern Hemisphere Using Six Years of IceCube Data. *Astrop. J.*, 833(1):3, 2016.
- [86] Eli Waxman and John N. Bahcall. Neutrino afterglow from gamma-ray bursts: 10^{18} eV. *The Astrophysical Journal*, 1:707–711, 2000.
- [87] S. Razzaque, P. Mészáros, and E. Waxman. High energy neutrinos from a slow jet model of core collapse supernovae. *Mod. Phys. Lett. A*, 20(31):2351–2367, 2005.
- [88] D. Eichler. High-energy neutrino astronomy - a probe of galactic nuclei. *Astrop. J.*, 232:106–112, 1979.
- [89] S. Adrian-Martinez et al. Measurement of the Group Velocity of Light in Sea Water at the ANTARES Site. *Astropart. Phys.*, 35:552–557, 2012.

- [90] J. R. Taylor. *An Introduction to Error Analysis: The Study of Uncertainties in Physical Measurements*. University Science Books, 1997.
- [91] D. Heck, J. Knapp, J. N. Capdevielle, G. Schatz, and T. Thouw. *CORSIKA: a Monte Carlo code to simulate extensive air showers*. 1998.
- [92] G. Carminati, M. Bazzotti, S. Biagi, S. Cecchini, T. Chiarusi, A. Margiotta, M. Sioli, and M. Spurio. MUPAGE: a fast atmospheric MUon GENERator for neutrino telescopes based on PArametric formulas. 2009.
- [93] D. J. L. Bailey. Genhen v5r1: Software documentation. ANTARES internal report ANTARES-Software/2002-004.
- [94] C. W. James. GENHEN release v7r6: ν_τ energy conservation, bug fixes, and changes to evt tags. KM3NeT internal report KM3NeT-SIM-2016-003.
- [95] D. J. L. Bailey. KM3 v2r1 User Guide, KM3 v2r1 User Guide. ANTARES internal report, ANTARES-Software/2002-004.
- [96] V. A. Kudryavtsev. Muon simulation codes MUSIC and MUSUN for underground physics. *Comput. Phys. Commun.*, 180:339–346, 2009.
- [97] M. Ambrosio et al. The MACRO detector at Gran Sasso. *NIMA*, 486(3):663 – 707, 2002.
- [98] Y. Becherini, A. Margiotta, M. Sioli, and M. Spurio. A parameterisation of single and multiple muons in the deep water or ice. *Astrop. Phys.*, 25(1):1 – 13, 2006.
- [99] Hep-spec web site. <http://w3.hepix.org/benchmarks/doku.php>.
- [100] Spec web site. <http://www.spec.org/>.
- [101] HEP-SPEC06 results for SL6 with gcc 4.4. http://w3.hepix.org/benchmarks/doku.php?id=bench:results_sl6_x86_64_gcc_445.

Appendix A: Use of the ANTS program (v3.0.0)

ANTS is a C++ program designed to run on a GNU/Linux system. It is a console program, i.e. it is meant to be configured and run via a command line interface – a *shell* running into a *terminal*.

It is common use for the command line interfaces to define *flags* and *arguments*. Flags can be in *short* or *long* form corresponding to a minus sign, `-`, followed by a single letter (or number) or to a double minus sign, `--`, followed by a word (or multiple words separated by underscore, `_`, or minus signs). Arguments typically follow a flag and are treated as parameters for a function. Indeed, the flags are used to activate (or deactivate) functionalities of a program, while arguments are used to set internal variables.

The following text reports about the current latest release, i.e. version 3.0.0. The information could change in future versions.

ANTS has two main running modes:

- the *configuration mode*, activated via the `--dump-defaults` command line flag, allows to retrieve the format and the default values of the parameters of the trigger algorithms specified as its argument(s);
- the *production mode*, the default one, is the mode meant to be used in production at the detector shore-station.

Additionally, the `-h/--help` and `-v/--version` command line flags allow to read the user help and the version of the software, respectively.

When in production mode, the program will run indefinitely, until it is stopped or a run-time error occurs⁴. In all other modes, the execution ends after having performed the proper action.

In production mode, the configuration is performed either via command line and by means of a `json`⁵ file that fully describes the trigger system setup.

⁴The spectrum of possible run-time errors is vast. It ranges from a software bug to external causes, e.g. a lost of communication with the ControlHost server. ANTS provides a very strong and powerful error reporting system so that when possible it will stop the execution writing a message to the user about the encountered error condition.

⁵It is a text-based data-interchange format. See <http://json.org>.

Embedded help

In the following snippet, the output of the `--help` is reported:

```
$ ./ants -h
Options:
-h [ --help ]           Print this help and
                        exit.
-v [ --version ]       Print the version and
                        exit.
-n [ --number-of-threads ] n (=10)  Initial number of
                        Reconstruction Units to
                        spawn.
-k [ --number-of-vertices ] n (=5)  Number of sub-timeslices
                        to divide the IQR in to.
-l [ --number-of-hits ] n (=10)     Minimum number of hits
                        in a centroid to
                        consider it.
-d [ --detector-file ] file.det[x]  Path of the file
                        containing detector
                        informations.
-s [ --server ] address              Remote address of the
                        ControlHost server.
                        Colon syntax allowed.
-t [ --tag ] tag (=IO_EVT)           ControlHost tag to
                        subscribe to.
-p [ --trigger-parameters ] file.json Configure the trigger
                        parameters.
--dump-defaults file.so ...          Show the default trigger
                        parameters for the given
                        plugins and exit
                        immediately.
```

It shows a description for each command line flag. Alternative long aliases to the short flags are reported inside square brackets. For example the `-h` and `--help` flags are equally accepted and have both the same effect. Next to the parameter, a placeholder may be present. It means that the flag accepts an argument. The latter can eventually have a default value, that, if present, is shown inside round brackets preceded by an equal sign `=`. In general, default parameters are reasonable and safe values.

Configuration mode

Each trigger algorithm must be implemented in a separate object, called *plug-in*. Detailed information about how to integrate a new algorithm in the ANTS' plug-in system are reported in Appendix B.

A plug-in is provided to the user in the form of a *shared object*, i.e. a binary file produced by the C++ compiler that implements the trigger algorithm. Shared objects are identifiable by the “.so” extension at the end of their file name.

Each trigger algorithm must internally provide an object that represents its configuration format, i.e. the name and structure of the parameters, and a default value for each trigger parameter. The default configuration is shown to the user by means of the `--dump-defaults` command line flag. Typing to a terminal the command:

```
$ ./ants --dump-defaults /path/to/the/shared/object.so
```

will print into the terminal the json-formatted representation of the default configuration. The `--dump-defaults` accepts multiple plug-in files at once, separated by spaces:

```
$ ./ants --dump-defaults object_1.so object_2.so object_3.so
```

The output of the:

```
$ ./ants --dump-defaults plugins/*.so
```

command would, at the current state, look like:

```
{
  "Plugin_0":
  {
    "so": "plugins/libhighlight.so",
    "parameters":
    {
      "NHits": "10000",
      "QualityThreshold":
      [
        "0.95",
        "0.1"
      ]
    }
  },
  "Plugin_1":
  {
    "so": "plugins/libhotspot.so",
    "parameters":
    {
      "NTracks": "2",
      "AngularAperture_degree": "10",
      "TimeWindow_us": "2000000",
      "QualityThreshold":
      [
        "0.95",
        "0.1"
      ]
    }
  },
  "Plugin_2":
  {
    "so": "plugins/libscaler.so",
```

```

    "parameters":
    {
      "Factor": "1",
      "QualityThreshold":
      [
        "0.95",
        "0.1"
      ]
    }
  }
}

```

At the top level, a name is assigned to a sub-block that configures a plug-in instance. The “so” property defines the path of the shared object file, while under the “parameters” the actual trigger parameters are listed. The format and values of the latter are completely defined by the developer of the plug-in. It is a developer’s duty to write them in an understandable and safe way. This procedure allows the user to have exact information about how to configure the trigger directly from the plug-in, without having to find the right documentation and to dig into it. This output can be redirected to a file and comfortably edited with any text editor in order to prepare the configuration for the production run. Each trigger algorithm can be instantiated multiple times within the same production run, by replicating the plug-in sub-blocks with different names. This allows to fine tune the same algorithm for different studies. The names can be freely changed and could be used by the underlying alert system. If two sub-blocks are mapped with the same name, only the last one appearing in the file is considered.

Production mode

For the production mode, the `-d/--detector-file`, `-s/--server` and `-p/--trigger-parameters` flags must be present on the command line. They do not have a default parameter, thus they must be provided by the user. An example of minimal command line for launching ANTS is:

```
$ ./ants -d km3net.detx -s controlhost.km3net-daq -p conf.json
```

Appendix B: How to implement a plug-in

As already stated in Appendix A, trigger algorithms are implemented into separated binary object files, whose names end with the “.so” extension.

API¹ bindings are provided for the C++ programming language only and are available through the `ants/plugin.hpp` C++ header file.

A class derived from the `ants::base_trigger` class must be present, as it is the actual interface with the trigger algorithm.

The `bool execute(ants::track const&)` member function must be implemented. This function is called each time a reconstruction unit returns a track, that is passed as its only argument.

The `ANTS_REGISTER_PLUGIN(class_name)` macro allows to ease the exposure of the trigger class to the ANTS, automatically defining two functions:

```
1 | extern "C" {  
2 |   ants::base_trigger* make_new(  
3 |     ants::configuration const& conf  
4 |   );  
5 |  
6 |   void destroy(ants::base_trigger* pbt);  
7 | }
```

These wraps around the constructor and the destructor of the newly defined class, properly disabling name mangling². In case of particular needs these functions can be manually implemented. In the case the macro is used, the class must implement a constructor that accepts the `ants::configuration` object directly.

A third function must be present where the the default configuration object is implemented:

¹Application Programming Interface

²Due to the C++ overloading feature function names in object files are different with respect to that in the source code. Hashes are prefixed and appended to the name in order to avoid clashes. On the other hand, the exact name must be known to correctly load the function from an external shared object file. For this reason, overload must be disabled for functions meant to be exported.

```
1 | extern "C" ants::configuration default_configuration();
```

The `ANTS_PLUGIN_DEFAULT_CONFIGURATION` macro eases the definition of this function, as shown below.

The returned `configuration` object must cope in format with the one expected to be passed to the `make_new` function, and its content is completely developer-defined.

Data structures

Many of the data structures present in the ANTS code use the Boost³ C++ library. The following types are actually `typedef`s of Boost's objects:

- `ants::configuration` → `boost::property_tree` ;
- `ants::chrono::seconds` → `boost::chrono::seconds` ;
- `ants::chrono::microseconds` → `boost::chrono::microseconds` ;
- `ants::chrono::nanoseconds` → `boost::chrono::nanoseconds` ;
- `ants::chrono::ticks` → `boost::chrono` -compatible 16 ns unit.

For them, the Boost website contains full and accurate documentation.

The `ants::track` object is defined as:

```
1 | namespace ants {
2 | struct track
3 | {
4 |     chrono::nanoseconds time;
5 |     Line line;
6 |     Metadata metadata;
7 | };
8 | }
```

where the `line` object carries the direction, application point, and quality parameters values, the `time` object is the median hit time of the cluster and `metadata` is a further field for other reconstruction values, currently (v3.0.0) filled with the `nclusterhits` field.

The interface for the `ants::Line` class is:

```
1 | class Line
2 | {
3 |     public:
4 | }
```

³www.boost.org

```

5 | // returns the number of centroids
6 | int npoints() const;
7 |
8 | // returns the direction
9 | geometry::Direction const& direction() const;
10 |
11 | // returns the application point
12 | geometry::Point const& point() const;
13 |
14 | // returns the quality parameter as a (q,p) pair
15 | std::pair<double, double> quality() const;
16 |
17 | // returns the Bravais-Pearson's linear correlation
18 | // coefficients, for each space coordinate
19 | geometry::vector3d const& bravais() const;
20 |
21 | // returns the pvalues of the BP linear correlation
22 | // coefficients, for each space coordinate
23 | geometry::vector3d const& pvalues() const;
24 | };

```

The `geometry::Point` and `geometry::Direction` are classes derived from `geometry::vector3d`, whose interface is:

```

1 | class vector3d {
2 |     public:
3 |         // default constructor
4 |         vector3d();
5 |
6 |         // copy constructor
7 |         vector3d(vector3d const& d);
8 |
9 |         // construct by components
10 |        vector3d(double cx, double cy, double cz);
11 |
12 |        // construct from double array of 3
13 |        explicit
14 |        vector3d(double const (&c)[3]);
15 |
16 |        // assignment operator
17 |        vector3d& operator =(vector3d const& d);
18 |
19 |        // x coordinate getter
20 |        double x() const;

```

```

21 |
22 |     // y coordinate getter
23 |     double y() const;
24 |
25 |     // z coordinate getter
26 |     double z() const;
27 |
28 |     // returns the square of the Euclidean modulus
29 |     double modulus2() const;
30 |
31 |     // returns the Euclidean modulus
32 |     double modulus() const;
33 | };

```

The `ants::geometry::Direction` class also provides the following member functions in addition to that provided by `ants::geometry::vector3d`:

```

1 | class Direction : public vector3d {
2 |     public:
3 |
4 |     // returns the x direction cosine
5 |     double cx() const;
6 |
7 |     // returns the y direction cosine
8 |     double cy() const;
9 |
10 |    // returns the z direction cosine
11 |    double cz() const;
12 |
13 |    // returns the normalized direction
14 |    Direction normalize() const;
15 | };

```

Plug-in example code

The content of an hypothetical `mytrig.cpp` would look like the:

```

1 | #include <ants/plugin.hpp>
2 |
3 | class MyTrigger : public ants::base_trigger
4 | {
5 |     // your private data go here
6 |
7 |     public:

```

```

8
9     explicit
10    MyTrigger(ants::configuration const& conf)
11    {
12        // initialisation code goes here
13    }
14
15    // return whether the trigger is set
16    bool execute(ants::track const& t)
17    {
18        // your algorithm goes here
19    }
20 };
21
22 ANTS_REGISTER_PLUGIN(MyTrigger);
23
24
25 ANTS_PLUGIN_DEFAULT_CONFIGURATION {
26     ants::configuration conf;
27     // initialise the configuration format
28     // and default parameters
29     return conf;
30 }

```

Notes for building the plug-in

The CMake⁴ tool controls the ANTS compilation. A `FindANTS.cmake` file is provided to help building plug-ins. It tries to find the installation directory of ANTS and, on success, it sets the `ANTS_FOUND` and `ANTS_INCLUDE_DIR` CMake variables. The `ANTS_SOURCE_DIR` variable can be set to the path of the ANTS source directory in order to help the search process.

Recalling the example in the snippet above, a CMake file would look like:

```

project(MyTrig CXX)
cmake_minimum_required(VERSION 2.6)

find_package(ANTS REQUIRED)

include_directories(${ANTS_INCLUDE_DIR})
add_library(MyTrig MODULE MyTrig.cpp)

```

⁴www.cmake.org